Interplanetary shock waves and large-scale structures: Ulysses' observations in and out of the ecliptic plane

J. A. González-Esparza,[1] A. Balogh, and R. J. Forsyth

Space ant] Atmospheric Physics Group, Imperial College, The Blackett Laboratory, London SW7 2BZ, UK

M. Neugebauer, and E. J. Smith

Jet Propulsion Laboratory, California Institute of Technology, M S 169-506, 4800 Oak Grow Drive, Pasadena, CA, 91109-8099.

J. L. Phillips

Los Alamos National Laboratory, P.O. Box 1663, MS D466, Los Alamos, NM 87545

Received _____—; accepted —-_— —-——.. — .

Submitted in the *Journal of Geophysical Research, 1995.*

Short title: SHOCK WAVES AND LARGE-SCALE STRUCTURES

[1]Now at Jet Propulsion Laboratory, California Institute of Technology, MS 169-506, *4800* Oak Grove Drive, Pasadena, CA. 91109-8099. *e-mail* : americo@jplsp.jpl.nasa.gov

Abstract.

We present a study of 153 fast shock waves and their relation to other large-scale features in the solar wind: corotating interaction regions (CIRs), interplanetary counterparts of coronal mass ejections (ICMEs) and the magnetic sector structure, observed by Ulysses from October 1990 to the south solar polar pass in the summer of 1994. This is a comprehensive statistical study of interplanetary shock waves and their possible causes between 1 and 5.4 AU, in particular, out of the ecliptic. We identify six different heliographic intervals with distinct dynamic characteristics and shock wave populations (transient and corotating shocks). We present maps of large-scale features, which provide a general context, to studies of particular events observed by Ulysses and a comparison] of Ulysses observations with results from other missions. From our analysis of the associations between interplanetary shocks and their possible causes we find that the strongest in-ecliptic shock waves were leading CIRS about 4-5 AU, The strongest out-of-ecliptic shock waves were attributed to diverse causes at about 20° south. We observed many quasi-parallel ($\theta_{B_n} < 45°$) corotating shocks; in fact, most of the corotating reverse shocks detected during the in-ecliptic trajectory were quasi-parallel. The correlation between transient forward shocks and ICMEs is similar to previous results within 1 AU: during the in-ecliptic trajectory Ulysses detected 25 ICMEs and 31 transient forward shocks, thirteen of which were associated with ICMEs. The out-of-ecliptic results show an analogous correlation. After the Jupiter fly-by we observed a large number of transient reverse shocks and they do not show any association with ICMEs. This type of shock, instead of being driven by supermagnetosonic plasma

clouds, might be produced by a different mechanism

1 Introduction

The aim of this paper is to describe the radial, heliographic and temporal variations of interplanetary shock waves and other large-scale structures detected by Ulysses from its launch in October 1990 to the south solar polar pass in mid 1994. We study the causes and the local parameters of the shock waves.

Fast interplanetary shock waves are classified into two categories depending on their possible causes: corotating shocks -attributed to interaction regions- and transient shocks (see e.g., the review by *Luhman* [1995] and references therein). Corotating shocks are produced by the interaction of fast solar wind overtaking slow solar wind in the interplanetary medium. These shocks are bound interaction regions and they are predominant features in the outer heliosphere (i.e. beyond 2 AU) (see e.g., the reviews by *Burlaga* [1984]; and *Smith* [1985] and references therein). Transient shocks are believed to be produced by fast coronal mass ejections (CMEs). These plasma clouds or CMEs propagate supermagnetosonically through the solar wind driving forward transient shocks as a supersonic airplane drives a hydrodynamic shock wave. The association between transient shocks (within 1 AU) and CMEs was established from CME observations by the Solwind coronagraph and the in-situ shock observations by Helios 1 [*Schewenn*, 1983; *Sheeley et al.*, 1983; *Sheeley et* d., 1985], Several papers have reported a good correlation between transient shocks (within 1 AU) and diverse post-shock signatures attributed to the interplanetary counterpart of coronal mass ejections (ICMEs) [*Klein and Burlaga, 1982; Borrini et al.* , 1982; *Cane et al.*, 1987;

Marsden et al., 1987; Gosling *et al.*, 1987; *Lindsay et al.*, 1994]. Following previous studies of Pioneer [*Smith* and *Wolfe*, 1976; Smith *and Wolfe*, 1977] and Voyager [*Gazis and Lazarus*, *1983; Burlaga et al., 1984]* observations, we present a comprehensive study of interplanetary shock waves and their possible causes n the outer heliosphere (to 5.4 AU).

The outline of this paper is as follows: in section 1.1 we briefly describe the Ulysses trajectory. In section 2 we explain how we defined and identified the different large-scale features studied in this work: fast shock waves, interaction regions, heliospheric current sheet (HCS) crossings and ICMEs. In section 3, based on the large-scale observations of interplanetary magnetic field (IMF) magnitude and solar wind radial velocity! we identify six intervals with distinct dynamics. In section 4 we show the maps of large-scale structures observed by Ulysses in and out of the ecliptic plane, These maps present the heliographic evolution of the different large-scale features. Section 5 discusses the results obtained from the analysis of the maps and the local parameters of the shocks, and section 6 presents our Conclusions.

1.1 Ulysses Trajectory

Figure 1 shows the Ulysses' heliographic coordinates (heliocentric distance and heliolatitude) for the period investigated (see *Wenzel et al.*[1992] for more details On the mission). The figure is divided into six intervals (A, B, C, I), E, F) that we will discuss in following sections. The in-ecliptic trajectory, from the Earth to Jupiter, lasted about 16 months and covered a wide distance range (from 1 AU to 5.4 AU) in a narrow

heliographic latitudinal range (±5° around the solar equatorial plane). On the other hand, the part of the out-of-ecliptic trajectory where most of the shocks were observed covered a significant range in heliolatitude (from — 5.5° to --38°) in a relatively narrow distance range (4.6 ± 0.8 AU). The in-ecliptic trajectory took place immediately after the maximum of solar cycle 22, while the high latitude phase took place during the declining phase of the cycle.

2 Identification of Large-scale Structures

This study is based on fast shocks waves, interaction regions, HCS crossings and ICMEs identified from Ulysses observations using data from the magnetic field and solar wind plasma experiments described by *Balogh et al. [1992]* and *Bame et* al. [1992] respectively. These observations are described in the following subsections.

2.1 Interplanetary Fast Shock Waves

A large number of fast shock waves were detected by Ulysses in the period covered by this work, These events were identified using the solar wind plasma and the magnetic field high-time resolution data, From October 1990 to the end of 1993, the magnetic field team identified 160 possible fast shock waves and *Balogh et al.* [1995a] published a comprehensive list based on the analysis of their local parameters. As it is denoted in their list not all these events were confirmed by both solar wind plasma and magnetic field data. So we chose the 146 shock waves list confirmed by both experiments. In 1994, we observed only seven shock waves before the south solar polar pass. This work

is based on the study of this set of 153 interplanetary fast shock waves detected by Ulysses. The shock lists can be found elsewhere [*González-Esparza*, 1995; *Burton et al.*, 1992 (in-ecliptic observations up to 4 AU); *Balogh et al.*, 1995a (in-ecliptic and out of ecliptic observations until the end of 1993); *Balogh et al.*, 1995b (shocks in 1994)].

2.2 Interaction Regions

From Pioneer 10 and 11 observations we know that interaction regions are predominant large-scale features in the outer heliosphere away from solar maximum [*Hundhausen and Gosling*, 1976; *Smith and Wolfe, 1976]*. Interaction regions can be recurrent structures called corotating interaction regions (CIRs)[*Smith and Wolfe, 1977],* or they can bc transient events [*Burlaga et* al., 1984]. An interaction region is characterized, in the in-situ measurements, by: *1)* its recurrence every solar rotation (if it is a CIR); *2)* a solar wind radial velocity profile showing that a fast solar wind stream is overtaking a slow solar wind stream (fast and slow solar winds have different characteristics); *3)* in the region between these two streams there is a well-defined compression region: high IMF magnitude, high solar wind density, high proton and electron temperatures; and 4) there is a strong shear flow at the stream interface [Gosling *et al.*, 1978], We identify the interaction regions by scanning the 27-day plots of radial velocity, plasma density and proton temperature together with the plots of IMF magnitude. Any compressional signature lasting less than about 1 day in our data series which was not associated with well-defined fast and slow solar wind streams, was not considered an interaction region but a different transient event.

2.3 Heliospheric Current Sheet crossings

A HCS crossing is characterized in the in-situ 1 MF measurements by an abrupt rotation of approximately 180° in the longitudinal 1 MF angle Φ. By convention a positive polarity is assigned to the IMF if the field vector is directed away from the Sun and a negative polarity if the field vector is directed towards tile Sun. For our study, we consider a change iu the IMF polarity observed by Ulysses as an HCS crossing if the ncw polarity lasted for at least 2 days. A change of magnetic polarity for just a few hours was not attributed to a new magnetic sector.

2.4 Interplanetary counterparts of Coronal Mass Ejections

The identification of ICMEs by in-situ spacecraft measurements is not as simple as for shocks, CIRs and HCS crossings, and can be debatable in many cases (see e.g., *Gosling* [1993] and references therein). To identify the ICMEs observed by Ulysses, wc used the best known signature attributed to ICMEs: a hi-directional streaming of suprathermal electrons accompanied by some plasma cloud signatures (proton temperature depression, high helium abundance, low ion beta, high thermal Mach number, IMF magnitude enhancement and cloudlike field rotations), *Phillips et al. [manuscript in preparation]* produced a comprehensive list of in-ecliptic ICME observations. We have used their list to study their large-scale context and their relationship to the interplanetary shock waves, The out-of-ecliptic ICMEs were identified based on similar criteria.

2.5 Classification of Int erplanet ary Shock Waves

Based on their location in our data series with respect to ICME or CIR events, interplanetary shocks were classified in three categories depending on their possible causes: *1)* corotating shocks; *2)* transient shocks followed by ICMEs; and *3)* transient shocks not easily or readily associated with ICMEs. "1'aide 1 summarizes this classification. 'The association between interplanetary shocks and CIRs is straightforward from the data. If we can identify the interaction regions confidently, we can identify the corotating shocks. However, different time intervals have been used to associate transient shocks with ICME events within 1 AU. It is not clear what is a 'reasonable' interval between the detection of the transient shock and the signature of its driver and how this is going to change with the heliocentric distance. 'I 'he spatial separation between the shock and its driver should depend on the driver's geometry and speed propagation, as well as the solar wind ambient conditions. in many ICME events start and stop times are uncertain from the data series. To associate a transient shock and an ICME in our study wc have taken into account,: the heliocentric distance of the event, the time difference between the transient shock and the ICME, the velocity profile of the event (the front of the ICME must be faster than the ambient solar wind in order to drive the shock), and the total pressure profile of the event (the front of the ICME must be 'pushing' the ambient solar wind if it is a supermagnetosonic plasma cloud).

3 Intervals of solar wind dynamics

In this section we review the large-scale solar wind dynamics observed during the in-ecliptic and out-of-ecliptic parts of the trajectory.

3.1 In-ecliptic Observations

Figure 2 shows three-hour averages of IMF magnitude and solar wind radial velocity during the in-ecliptic trajectory. This trajectory can be broadly divided into two intervals (A and B) with different large-scale characteristics:

Interval A: from October 1990 (day 90:294) at 1 AU to April 1991 (day 91:1 17) when Ulysses was approaching 2,9 AU, During this interval the 1 MF magnitude was highly variable with peaks associated with transient events. Before the large peak in March 1991, the solar wind did not show quasi-stat ionary fast streams (see bottom panel in figure 2), but rather low-amplitude slow solar wind streams of about 380 km/s mean speed [*Bame et* al., 1993]. The most remarkable large-scale events occurred in March 1991 (between days 91:062-91 :084) at a distance of about 2.5 AU, when abrupt increases in solar wind speed, from about 380 km/s to 900 km/s, were associated with a major series of interplanetary shocks and ICMEs *[Phillips et al., 1992]. Balogh et al. [1993]* suggested that the high rate of transient activity detected by Ulysses through this interval was related to changes in coronal field structure associated with the reversal of the polar fields in 1990. The March 1991 events observed by Ulysses have been discussed in several papers (e.g., *Geophys. Res. Lett., 19,* June 19, 1992).

Interval B: from April 1991 (day 91:118) to the Jupiter fly-by in February 1992 (day 92:032) at 5.4 AU, In this interval, quasi-stationary fast solar wind streams appearing in every solar rotation produced a significant change of dynamics. In the top panel (figure 2) well-defined regions of high IMF magnitude were separated from low IMF values, a characteristic of CIRS followed by rarefaction regions. As expected from previous observations by Pioneer [*Smith and Wolfe*, 1977] and Voyager [*Gazis and Lazarus*, 1983] in similar heliocentric ranges, the dynamics were dominated by CIRs.

3.2 Out-of-ecliptic Observations

Figure 3 shows the large-scale observations of IMF magnitude and solar wind radial velocity during the out-of-ecliptic part of the trajectory. The two most significant changes in solar wind dynamics in these observation is arc: the 'appearance' of very fast streams from the south coronal hole in July 1992 [*Bame et* al., 1993]; and the 'disappearance' of the magnetic sector structure in May 1993 [*Smith et al.*, 1993]. Based on these two events, this trajectory has been divided into four intervals (C, D, E and F):

Interval C: from the Jupiter fly-by in February 1992 (about day 92:055) at 5.4 AU and 6° south, to the 'appearance' of the fast stream in July 1992 (about day 92: 184) at 5.3 AU and 13° south. This is a complex interval characterized by a series of ICMEs and transient activity.

Interval D: from July 1992 to the 'disappearance' of the sector structure in May 1993 (about day 93:105) at 5.1 AU and 28° south. This interval is characterized by the fast solar wind stream (up to 800 km/s) and regular CIRs. As *Bame et al.* [1993]

reported, this fast stream coming from the south coronal hole was observed for 14 successive solar rotations from July 1992 through June 1993. in November 1992 (day 92:313) an ICME occurred with the fastest solar wind measured so far by Ulysses -nearly 1000 km/s- [Phillips *et al.*, 1994].

Interval E: from about the disappearance of the magnetic sector structure at Ulysses to the 'disappearance' of slow solar wind streams in September 1993 (about day 93:261) at 4.3 AU and 38° south. Coincidentally with the disappearance of the magnetic sector structure, the minimum in solar wind speed rose and the interaction between the streams became weaker. Although this interval was dominated by interaction regions as the previous one, the shock population presented dramatic changes.

Interval F: from September 1993 to the south solar polar pass in the summer of 1994. The streams of slow solar wind disappeared and the whole region was filled by the fast stream from the south coronal hole. As expected close to the solar minimum, the large-scale dynamics at high-latitudes was practically nil.

High-latitude observations brought unexpected discoveries of solar wind dynamics and heliospheric shocks: the disappearance of forward shocks in interval E and three observations of an 'over-expanded CME' producing a shock pair reported by Gosling *et al.* [1994a] and *Gosling et al.* [1994b] in intervals E and F.

Disappearance of Forward Shocks at High Heliolatitudes

Ulysses found that after the disappearance of the magnetic sector structure forward shocks were absent at the leading edge of interaction regions, however, reverse

shocks continued to be present at the trailing edge of these interaction regions. These observations have been described in detail by Gosling *et al.* [1993] and *Balogh et al.* [1995a]. Gosling *et* al. [1993] and *Pizzo and Gosling* [1 994] suggested that this phenomenon can be explained by the three-dimensional model of MHD corotating flows developed by *Pizzo.* This model, assuming a simplified tilt cd bipolar geomet ry valid only close to the solar minimum, predicts that the Cl R fronts will be tilted with respect to the solar equator. l'he front of the CIR points towards the ecliptic plane while the trailing edge points towards high heliolat itudes (south or north depending on the coronal hole that produced the interaction region). This geometry causes the front of the CIR to develop stronger close to the solar equatorial plane while the trailing edge of the CIR develops stronger at higher latitudes. Cl [i-forward shocks are very strong at low latitudes, but they are weak and unlikely at nigh latitudes. CIR-forward and CIR-reverse shocks evolve in a different way in different heliographic locations.

Recently *Burton and Smith [unpublished manuscript],* applying magnetic coplanarity, and *Riley et al. [1995],* applying velocity coplanarity, found that the shock normal directions of the corotating shocks observed by Ulysses at mid-heliolatitudes in 1992 satisfied, in most of the cases, the predictions by the three-dilncnsional model of corotating flows by *Pizzo.*

4 Maps of Large-Scale Structures in the Solar Wind

This section presents the maps of large-scale features, consisting of chronological rows of 27 days during the in-ecliptic trajectory and 26 days during the out-of-ecliptic

trajectory, Although the apparent solar rotation period observed by Ulysses might vary between 24 and 31 days (depending on the sideral rate of the corona, the latitude and the orbital motion of the spacecraft), these two formats represent, on average, a good approximation to the solar rotation period relevant to the large-scale structures discussed in this paper. Every row or solar rotation observed by Ulysses (SRU) is numbered. 'l'he first SRU starts at the time of the magnetic field experiment switch-on in October 1990 and following SRUs were numbered consecutively until the end of 1993.

4.1 In-Ecliptic Observations

Figure 4 shows the map of large-scale structures in the solar wind during the in-ecliptic trajectory. Now we discuss the two intervals (A and B) that we defined n section 3.1:

4.1.1 Interval A

Interval A (from SRU 1 to 7 in figure 4) is characterized by transient events. Note the unusual activity in SRU 6 corresponding to the March 1991 events. There was no other period during the whole mission when Ulysses detected so many shocks (8) and ICMEs (6) in a single solar rotation. We detected 14 ICMEs in the whole interval, seven of them were identified as drivers of forward transient shocks (in SRU 2, 3, 5, 6 and 7). In SRU 6 we observed in two cases a transient shock inside an ICME.

Only one well-formed interaction region was observed. This event was detected at 1.4 AU (in SRU 3) and it was bounded by only a reverse shock. The Heliospheric

Current Sheet (HCS) was warped. The magnetic sector structure presented a four-sector pattern in SRU 2, 5 and 6 and a six-sector pattern in SRU 3 and 4.

We observed 22 interplanetary shocks, giving on average about 3.1 shocks per solar rotation. Table 2 summarizes the relation between the shocks and their possible causes. This interval was dominated by transient forward shocks: 91 per cent of the total were transient forward shocks. About 35 percent of these transient forward shocks were associated with ICME drivers. Only two reverse shocks were detected.

4.1.2 Interval B

Interval B (from SRU 8 to 18 in figure 4) shows a significant change with respect to interval A: reverse shocks and interaction regions were present in every solar rotation. We observed 18 CIRs, corresponding on average to more than one CIR per SRU (1.6). Most of the CIRS were bound by forward-reverse shock pairs, however, three CIRs were not trail by reverse shocks (in SRU 9, 11 and 18) and two CIRS were not preceded by forward shocks (in SRU 15 and 16). A particular feature of the CIRS observed in this interval were the four CIRS preceded by two forward shocks. Figure 5 shows two examples of these events. In both cases the second forward shock is moving supermagnetosonically through the downstream region of the first forward shock, implying that eventually the second shock is going to overtake the first one (assuming that both shocks are propagating approximately in the same direction). The stream interface is not well-defined inside both interaction regions. As far as we know, there are no reports of similar observations by Pioneer or Voyager in the same heliocentric

range. The two corotating forward shocks were separated in time between 0.5 and 9.0 hours in the four cases. One of these CIRs (in SRU 8) was produced by a fast stream carrying negative IMF, while the other three (in SRU 9, 12 and 15) were produced by fast streams carrying positive IMF.

In the first two SRU of this interval (8 and 9) t] ıe HCS was warped and there was a four-sector pattern similar to the previous interval A. Afterwards the sector pattern became simpler and changed to a predominant two-sector structure (SRU 10, 11, 13, 14, 15, 16 and 17) and opposite polarity sectors had approximately equal duration.

We identified 11 ICMEs; six of them were identified as drivers of transient forward shocks (in SRU 9, 12, 13, 15,16 and 17). One ICM E was observed inside a CIR in sRu 14.

Forty-eight shock waves were detected, corresponding to about 4.4 shocks per solar rotation. Although the rate of transient forward shocks per solar rotation decreased from about 2.9 in interval A, to about 1,0 in this interval, the total rate of shocks per SRU was higher. 'I'able 2 summarizes the relation between shocks and their possible causes. About 74 percent of the shocks were attributed to CIRs and only 26 percent were classified as transient events. About 54 percent of the transient forward shocks were associated with an ICME driver. We did not observe transient reverse shocks.

4.2 Out-of-Ecliptic Observations

Figure 6 shows the map of large-scale structures in the solar wind during the out-of-ecliptic trajectory using the same format as figure 4, but every row or SRU

corresponds to 26 days, We now discuss the four intervals (C, D, E, l?) that we defined in section 3,2.

4.2.1 Interval C

Interval C covers the first part of the Ulysses out-of-ecliptic trajectory, from SRU 19 to 23 in figure 6. This interval is characterized by transient events. We identified 9 ICMEs during this short interval; only in March 1991 we did observe a higher rate of transient activity, Presumably related to the series of ICMEs, the HCS was warped and there were successive solar rotations with two-sector and four-sector patterns. SRU 20 is the only example, beyond 3 AU, of an SRU without an interaction region. It is possible that this also was related to the series of ICMEs preventing the formation of interaction regions.

We detected 17 heliospheric shocks, corresponding to about 3.4 shocks per solar rotation. This is the only interval beyond 3 AU where we observed more ICMEs than CIRS and more transient shocks than corotating shocks. Four transient forward shocks were associated with ICME drivers (in SRU 19, 20 and 21). We detected three transient reverse shocks (in SRU 19, 20 and 22) and they were not associated with ICMEs (see table 2).

4.2.2 Interval D

Interval D begins with the appearance of the fast stream (about 800 km/s) in SRU 24 and ends with the disappearance of the magnetic sector structure in SRU 34

(figure 6). This interval was characterized by a predominant two-sector pattern. In SRU 24 the positive magnetic polarity almost, disappeared, presumably associated with the fast ICME in the middle of the solar rotation. Six ICMEs were identified, four of them were associated with transient forward shocks (in SRU 24, 26 , 28 and 30),

We observed 18 CIRS and the rate of CIRS per solar rotation is about the same as in interval B. Note however, that only two interaction regions were produced by the north coronal hole (in SRU 26 and 27) and this CIR disappeared abruptly at 18° south. The predominant CIR was produced by the south coronal hole and was observed in all SRU (24-33). Fourteen CIRS were led by forward shocks and thirteen CIRS were trail by reverse shocks. We did not observe double forward shocks leading CIRs in this interval.

We observed 40 shocks. Sixty-seven percent of them were associated with CIRs and the rest were classified as transient shocks (see table 2).

4.2.3 Interval E

Defined from SRU 35 to 40 in figure 6, this interval started after the last HCS crossing in April 1993 and the minimum of solar wind speed rising to values of about 550 km/s (figure 3). The shock population had dramatic changes: all the CIRs were trail by reverse shocks and there were just two forward shocks (see table 2).

We detected six ICMEs in this interval. In SRU 37 we observed an 'over-expanded CME' bounded by a shock pair as reported by Gosling *et al.* [1994a]. Apart from this event, no transient shocks were associated with ICM Es.

We identified 11 CIRs, corresponding on average to about 1.8 CIRS per solar

rotation. This is the highest rate of CIRS in the whole study and it is surprising since all these CIRs were produced within fast streams originating from the south coronal hole. In the simplified tilted geometry assumed by the global model of corotating flows [*Pizzo*, 1991; *Pizzo*, 1994] only one CIR is produced by the south coronal hole (and another by the north coronal hole) per solar rotation. However, Ulysses observed two or three CIRs in several rotation periods. All the CIRS were trail by reverse shocks and only one CIR was preceded by a forward shock. Contrary to the abrupt disappearance at Ulysses of the CIR produced by the north coronal hole in interval D, the CIRs produced by the south coronal hole disappeared gradually.

4.2.1 Interval F

The last interval is defined from the disappearance of the slow solar wind stream. At the beginning of the interval we observed two transient reverse shocks (in SRU 41 and 42). In 1994 (not shown in the figure 6) we observed two 'over-expanded CMES' (as the one in SRU 37) bounded by shock pairs [*Gosling et al.*, 1994b] and three reverse shocks, two of them attributed to interaction regions [*Balogh et al.*, 1995 b]. These nine shock waves (seven reverse and two forward) were the only shock waves confirmed from September 1993 to the south solar polar pass in mid-1994 (see table 2).

5 Summary and Discussion

5.1 In-Ecliptic Observations

In the first instance, the in-ecliptic shock observations were closc to our expectations based on those by Pioneer and Voyager: a) wc detected more forward shocks than reverse shocks; b) within 3 AU most shocks observed by Ulysses were attributed to transient events associated with solar activity and c) beyond 3 AU most of the shocks were attributed to CIRs. However, our discussion of the large-scale observations by Ulysses leads to the following points:

1) Heliographic changes in the shock population: In interval A less than 5 percent of the shocks were attributed to CIRs, while in interval B, associated with the change in dynamics, 74 percent of the shocks were attributed to CIRs. Although most of the shocks beyond 3 AU were corotating, there is a significant population of transient shocks. Corotating and transient shocks in this heliocentric range, in principle, can be distinguished by their large-scale profiles of solar wind plasma and IMF data.

2) Interaction Regions: the first CIR observed by Ulysses was at about 1.4 AU (in SRU 3) and was accompanied by only a reverse shock. The second well-formed CIR observed by Ulysses did not appear until interval B (in SRU 8) at about 2.85 AU and was bound by a shock pair. These observations, as the variation in shock population, were related to the change in solar wind streams from interval A to interval B (more a temporal than a heliocentric effect). Figure 7 shows the heliocentric evolution of the duration of the interaction regions during the in-ecliptic trajectory. In interval B

the pattern of fast and slow solar wind streams was stable and interaction regions increased their duration with the heliocentric distance denoting their expansion. The early interact ion regions were produced by fast streams carrying negative IMF, and from about 3,5 AU the large scale dynamics was dominated by fast streams carrying positive IMF.

3) Shock local parameters: An MHD shock wave is characterized by two parameters: θ_{B_n} (the angle between the shock normal direction and the upstream magnetic field) and the Mach number M_s (the normalized propagation speed of the shock wave in the medium) (see e.g., *Kennel et* al. [1985] and references thei ein). Figure 8, based on the shock list by *Balogh et al.* [1995a], shows θ_{B_n} frequency distributions for three types of shock waves: transient forward, corotating forward and corotating reverse shocks, observed during the in-ecliptic trajectory. Most of the forward shocks (transient and corotating) were quasi-perpendicular (θ_{B_n} > 450). However, most of the corotating reverse shocks were quasi-parallel (θ_{B_n} < 450). Although in short intervals of 1 to 5 minutes the IMF can have practically any direction; this result is contrary to our idea that most of the corotating shocks are quasi-perpendicular. Figure 9, based on the same shock list, shows the heliocentric variation of the Mach numbers of the three types of shocks presented in the previous figure. Transient forward shocks have a diverse collection of M_s from very weak shocks ($M_s \sim 1$) to relative strong interplanetary shocks (M_s about 2.8). Corotating forward shocks were, in general, stronger than corotating reverse shocks. The strongest shocks during the in-ecliptic trajectory were detected about 4-5 AU leading interaction regions.

4) ICMEs preceded by transient shocks: During the in-ecliptic trajectory, Ulysses detected 25 ICMEs ant] 13 of them were associated to transient forward shocks. This means that 52 percent of the ICMEs were associated with shocks. This result is similar to previous reports at 1 AU: Gosling *et* al. [1987] studied 49 ICMEs (based on hi-directional electron flows) detected by 1 SEE 3 from 1978 to 1979 (maximum cycle 20), and they found that about half of their ICMEs were preceded by transient shocks, *Marsden et al.* [1987] studied 66 ICMEs (based on bi-directional flows of low energetic protons) detected by the same spacecraft about the same period, and they found that 47 percent of their ICMEs were associated with transient shocks, *Klein and Burlaga* [1982] studied 45 magnetic clouds observed at 1 AU from 1967 to 1978 (solar cycle 20), and they found that 29 percent of their ICMEs were preceded by shocks.

5) Transient forward shocks associated with ICMEs: We detected 31 transient forward shocks during the in-ecliptic trajectory, 13 of them were associated with ICMEs. This associated fraction of 42 percent is similar to that found in previous studies within 1 AU: *Borrini et al.* [1982] studied 103 forward shocks observed by IMP from 1971 to 1978 (declining phase of cycle 20- ascending phase of cycle 21) and they found that 40 percent of their shocks were associated with ICMEs (identified by helium enrichments). *Lindsay et al. [1994]* studied 45 forward shocks detected by PVC) from 1979 to 1988 (maximum cycle 21- ascending phase of cycle 22) and they found that 80 percent of their transient shocks were associated with ICMEs (magnetic clouds signatures). Gosling *et al.* [1987] found that about 40 percent of the transient shocks that they studied were followed by ICMEs.

The 58 percent of transient forward shocks that we observed without an ICME associated might be explained by geometrical effects, i.e., the extent of the transient shock was far larger than its driver (see e.g., the papers referred to earlier). On the other hand, it is also possible that in the outer heliosphere the s] iock separates from its driver.

5.2 Out-of-Ecliptic Observations

Immediately after the Jupiter fly-by we began to observe significant large-scale changes in shock population and solar wind dynamics:

1) Interaction regions: Figure 10 shows the latitudinal evolution of the CIR duration during the out-of-ecliptic trajectory. In the beginning we observed very extended interaction regions, The CIR produced by fast solar wind from t he north coronal hole disappeared abruptly at 18° south. From about 20°, when all the CIRs were produced by the south coronal hole, the CIRS decreased their duration with latitude. This latitudinal decrease in CIR duration can be explained by the rise in slow solar wind velocity in interval E (which made the stream interactions weaker) and three-dimensional effects that cause high-latitude CIRs to steep at larger heliocentric distances than low-latitude CIRS [*Pizzo*, 1982], In interval E Ulysses detected two or three interaction regions per solar rotation produced by fast streams with negative IMF. This phenomenon might be related with a contort neutral sheet. Even close to the solar minimum, the two polar coronal holes are not necessarily symmetric and occasionally appear small coronal holes at low latitudes that deform the shape of the neutral sheet, For example, during the fast

latitude scan in 1995 (passing from the south to the north solar hemisphere), Ulysses detected several interaction regions and four magnetic sectors that were associated with four coronal holes: two asymmetric polar coronal holes, and two small equatorial holes with opposite polarities [*Smith et* cd., 1995]. As the region of slow solar wind is related with the neutral sheet, an irregular shaped neutral sheet might cause multiple interaction regions per solar rotation (even if there are only two coronal holes) and local variations in the three-dimensional geometry of the interaction regions. It is possible that a generalization of the three-dimensional simulations of corotating flows by *Pizzo* might explain these phenomena.

2) Shock local parameters: Figure 11 shows the θ_{B_n} frequency distributions (based on the shock list) for the four types of shock waves detected during the out-of-ecliptic trajectory: transient forward, transient reverse, corotating forward and corotating reverse shocks, Contrary to in-ecliptic results shown in figure 8, we did not observe a clear difference or tendency between corotating forward and reverse shocks, but they seem distributed in quasi-parallel and quasi-perpendicular values. Figure 12 shows the scatter plot of the Mach number (based on the shock list) against latitude for the four types of shocks detected after the Jupiter fly-by The strongest shocks were observed in intervals C and D attributed to different causes. In a similar way as the decrease in CIR duration shown in figure 10, the strength of the shocks decayed after 20° south. *Burton and Smith [unpublished manuscript],* pointed out that this peak in shock strength at about 20° was related to the maximum in energetic particle intensity observed by Ulysses after the Jupiter fly-by.

3) Transient reverse shocks: after the Jupiter fly-by we observed a surprisingly large number of transient reverse shocks, Reverse shocks are rarely observed within 1 AU and most of them are attributed to CIRS [*Gosling et al., 1988].* Based on observations within 1 AU, it is usually assumed that transient shocks are mostly forward, produced by the supermagnetosonic propagation of ICMEs through t he solar wind. However, there was no association of transient reverse shocks and ICMEs in the whole study (excepting the reverse shocks associated with 'over-expanded CMEs'). Figure 13 shows two examples of transient reverse shocks detected by Ulysses after the Jupiter fly-by, The first example, detected on day 92:142 (SRU 22), is propagating against slow solar wind ($V_r \leq 415$ km/s), while the second event, detected on day 93:085 (SRU 34), is propagating against fast solar wind ($V_r \geq 730$ km/s). Recent MHD simulations of corotating flows [*Pizzo*, 1982; *Pizzo*, 1991; *Hu*, 1993] predict that corotating reverse shocks form earlier than corotating forward shocks. The two shocks, forward and reverse, play different roles in the physics of the interaction between fast and slow MHD streams. Depending On the geometry and the ambient conditions the two shocks form and evolve in a different way. *Pizzo* illuminated the three-dimensional effects on the M HI) stream interface, which seems to explain many of the phenomena observed by Ulysses at high latitudes. It might be possible that these physical effects: the earlier formation of the corotating reverse shocks and the geometry of the stream interface, would explain the numerous transient reverse shocks that we observed after the Jupiter fly-by, In this case these transient reverse shocks would be equivalent to 'thin' interaction regions produced by temporal variations of the fast and slow solar wind sources.

6 Conclusions

We subdivided the Ulysses trajectory into different intervals with particular dynamic characteristics. Figure 14 summarizes the four classes of heliospheric shock waves that wc detected in five intervals. These inter vals were dominated by different types of shock waves. The shock population and their characteristics depend on the heliographic location and the solar wind dynamic conditions. The dramatic change in shock population from interval A to interval B was produced by a change in the solar wind streams more than an effect produced by the heliocentric distance. Interval C shows that most of the interplanetary shock waves in the outer heliosphere are not necessarily corotating shocks, but we cannot separate the analysis of interplanetary shock waves from their large-scale context. 1 low arc the large-scale dynamics and the shock population affected by the solar cycle? A study comparing Pioneer 10 and 11, Voyager 2 and 1 and Ulysses observations from 1 to 5 AU is under way [*González-Esparza and Smith, manuscript in preparation].*

Shock Local Parameters

During the in-ecliptic trajectory the strongest shock waves were forward corotating shocks detected about 4-5 AU. The strongest transient shocks were observed in March 1991 associated with ICMEs. During the out- of-ecliptic trajectory the strongest shocks were observed about 20° south, Contrary to our expectations, we detected many quasi-parallel corotating shocks, During the in-ecliptic trajectory most of the corotating reverse shocks were quasi-parallel. These results might be produced by coincidental IMF

fluctuations or/and local variations of the shock nor real, however, it is possible that they are related to three-dimensional effects that we just recently begun to investigate,

Transient Forward Shocks Associated with ICMEs

We have studied for the first time the correlation between transient shocks and ICMEs in the outer heliosphere (to 5.4 AU), We obtained similar results as previous studies within 1 AU: transient forward shocks and 1 CMEs seem to be well correlated in the outer heliosphere (to 5.4 AU).

Transient reverse shocks

A large number of transient reverse shocks were observed by Ulysses after the Jupiter fry-by, These transient reverse shocks showed no correlat ion with ICMEs. These observations suggest that this type of shock wave is produced by a different mechanism than the transient shocks observed within 1 AU, which are mostly forward and which we believe are produced by supermagnetosonic plasma clouds. These transient reverse shocks might be produced by transient variation of the fast and the slow solar wind sources producing 'thin' interaction regions which only develop reverse shocks at these heliographic locations. New MHD simulations might illuminate the cause of these transient reverse shocks observed by Ulysses.

Acknowledgments. We are grateful to one of the refeeres who provide us useful suggestions and to Tim Horbury for his help in producing the maps of large-scale structures in the solar wind. J. A. G-E. is grateful to the Universidad National Autónoma de México

for financial support at Imperial College and to the National Research Council for financial support at JPL. Ulysses related work at Imperial College is supported by the UK Particle Physics and Astronomy Research Council, and, at the Jet Propulsion Laboratory, California Institute of '1'ethnology, by the National Aeronautics and Space Administration.

References

Balogh, A., T. J. Beck, R. J. Forsyth, P. C. Hedgecok, R. J. Marquedant, E. J. Smith, D. J. Southwood, and B. T, Tsurutani, The magnetic field investigation on the Ulysses mission: instrument ation and preliminary scientific results. *Astron. Astrophys. Suppl. Ser.*, 92, 221-236, 1992.

Balogh, A., G. Erdos, R. J. Forsyth, and E. J. Smith, The evolution of the interplanetary sector structure in 1992. *Geophys. Res. Lett., 20, 2331-2334,* 1993.

Balogh, A., J. A. González-Esparza, R. J. Forsyth, M. E. Burton, B. E. Goldstein, E. J. Smith and S, J. Bame, Interplanetary shock waves: Ulysses observations in and out of the ecliptic plane. *Space Science* Reviews, 72, 171-180, 1995a.

Balogh, A., E. J. Smith, B. T. Tsurutani, D. J. Southwood , R. J. Forsyth, and T. S. Horbury, The heliospheric magnetic field over the south polar region of the sun. Science, 268, 1007, 1995b.

Bame, S. J., D. J. McComas, B. L. Barraclough, J. L. Phillips, K. J. Sofaly, J. C. Chavez, B. E. Goldstein, and R. K. Sakurai, The Ulysses mission solar wind plasma experiment. *Astron. Astrophys. Suppl. Ser.,* 92, 237-265, 1992.

Bame, S. J., B. E. Goldstein, J. T. Gosling, J, W. Harvey, D. J. McComas, M. Neugebauer and J. L. Phillips, Ulysses observations of a recurrent high-speed solar wind stream and the heliomagnetic streamer belt. *Geophys. Res. Lett., 20, 2323, 1993.*

Borrini, G., J. T. Gosling, S. J, Bame, and W. C. Feldman, An analysis of shock wave disturbances observed at 1 au from 1971 through 1978. *J. Geophys. Res., 87,4365-4373, 1982.*

Burlaga, L. F., MHD processes in the outer heliosphere. *Space Science Reviews, 39, 255-316,*

1984.

Burlaga, L. F., I,. W. Klein, R. P. Lepping, and K. W. Behannon, Large scale interplanetary magnetic fields: Voyagers 1 and 2 observations between 1 au and 9.5 au. *J. Geophys. Res.*, 89, 10659-10668, 1984.

Burton, M. E., E. J. Smith, B. E. Goldstein, A. Balogh, R. J. Forsyth, and S. J. Bame, Ulysses: interplanetary shocks between 1 and 4 au. *Geophys. Res. Lett.*, *19*, 1287, 1992.

Cane, H. V., N. R. Sheeley, and R. A. Howard, Energetic interplanetary shocks, radio emission, ant] coronal mass ejections. *J. Geophys. Res.*, *92, 9869-9874,* 1987.

Gazis, G. R., and A. J. Lazarus, The radial evolution of the solar wind, 1- 10 au. in *Solar Wind Five,* M. Neugebauer, editor, NASA headquarters and JPL, 1983.

González-Esparza, J. A., Study of heliospheric shock waves observed by Ulysses magnetometer in and out of the ecliptic plane, Ph.D. thesis, *Imperial College,* London, 1995.

Gosling, J. T., J. R. Asbridge, S. J. Bame, and W. C. Feldman, Solar wind stream interfaces, *J. Geophys. Res.*, *83, 1401-1412,1978.*

Gosling, J. T., D. N. Baker, S. J. Bame, W. C. Feldman, R. D. Zwickl, and E. J. Smith, Bi-directional solar wind electron heat flux events. *J. Geophys. Res., 92, 8519-8535, 1987.*

Gosling, J. T., S. J. Bame, E. J. Smith, and M. Burton, Forward -reverse shock pairs associated with transient disturbances in the solar wind at 1 au. *J. Geophys. Res., 93, 8741-8748, 1988.*

Gosling, J. T., The solar flare myth. *J. Geophys. Res., 98, 18937-18949, 1993.*

Gosling, J. T., S. J. Bame, D. J. McComas, J. L. Phillips, V. J. Pizzo, B. E. Goldstein, and M. Neugebauer, Latitudinal variation of solar wind corotating stream interaction

regions: *Ulysses. Geophys.Res.Lett., 20, 2789 -27'92,* 1993b.

Gosling, J. T. , S. J. Bame, D. J. McComas, J. L. Phillips, E. E. Scime, V. J. Pizzo, B. E. Goldstein, and A. Balogh, A forward -reverse shock pair in the solar wind driven by over-expansion of a coronal mass ejection: Ulysses observations. *Geophys.Res.Lett., 21, 237,* 1994a.

Gosling, J. 'i'. , 1). J. McComas, J. L. Phillips, 1,. A. Weiss, V. J. Pizzo, B. E. Goldstein, and R. J. Forsyth, A new class of forward-reverse shock pairs in the solar wind. *Geophys. Res. Lett., 21, 2271,* 1994b.

Hu, Y. Q., Evolution of corotating stream structures in the heliospheric equatorial plane. *J. Geophys. Res.,* 98, 13201-13214, 1993.

Hundhausen, A. J., and J. T. Gosling, Solar wind structure at large heliocentric distances: an interpretation of Pioneer 10 observations, *J. Geophys.Res., 81,* 1436-1440, 1976.

Kennel, C. 1?,, J. P. Edrnison, and 1. Hada, A quarter century of collisionless shock research, *In Collisionless Shocks in the Heliosphere: A Tutorial Review, R. G.* Stone and B. T. Tsurutani, editors, *Geophysical Monograph,* 34, 1,1985

Klein, L. W., and L. F. Burlaga, Interplanetary magnetic clouds at 1 au. *J. Geophys. Res.,* 87, 613-624, 1982.

Lindsay, G. M., C. T. Russell, J. G. Luhmann, and P. G azis, On t he sources of interplanetary shocks at 0.72 au. *J. Geophys. Res., 99,* 11-17, 1994.

Luhmann, J. G., Sources of interplanetary shocks. COSI 'AR, *Adv. Space Res.,* 16,1995.

Marsden, R. G., T. R. Sanderson, C. Tranquilly, and K. -P, Wenzel, ISEE 3 observations of low-energetic proton hi-directional events and their relation to isolated interplanetary magnetic structures. *J. Geophys.Res., 92,* 11009-11019, 1987.

Phillips, J. L., S. J. Bame, J. T. Gosling, D. J. McComas, B. E. Goldstein, E. J. Smith, A. Balogh, and R. J. Forsyt h, Ulysses plasma observations of coronal mass ejections. *Geophys. Res. Lett., 19, 1239, 1992.*

Phillips, J. L., A. Balogh, S. J. Bame, B. E. Goldstein, J. T, Gosling, J. T. Hoeksema, D. J. McComas, and M. Neugebauer, Ulysses at 50(' south: constant immersion in the high-speed solar wind. *Geophys. Res. Lett., 21,* 1105-1108, 1994.

Phillips, J. L., S. J. Bame, W. C. Feldman, J. T. Gosling, C. M. Hammond, D. J. McComas, 11.13. Goldstein, Ulysses solar wind plasma obsei vat ions during the declining phase of solar cycle 22. COSPAR, *Adv.* Space *Res., 16,* (9)85, 1995.

Pizzo, V. J., A three-dimensional model of corotating streams in the solar wind. *J. Geophys. Res.,* 87, 4374-4394, 1982.

Pizzo, V. J., The evolution of corotating stream fronts near the ecliptic plane in the inner solar system. 2. three-dimensional tilt cd-dipole fronts. *J. Geophys. Res.,* 96, 5405-5420, 1991.

Pizzo, V J., Global, quasi-steady dynamics of the distant solar wind. 2. origin of north-south flows in the outer heliosphere. *J. Geophys. Res.*, 99, 4173,1994.

Pizzo, V. J., and J. T. Gosling, 3-D simulations of high latitude interaction regions: comparation with Ulysses observations. *Geophys. Res. Lett., 21, 2063,1994.*

Riley, P., J. T. Gosling, L. A. Weiss, and V. J. Pizzo, The tilts of corotating interaction regions at mid heliographic latitudes. Program/abstracts, *International Solar Wind 8 Conference,* p.. 90, Dana Point, CA, 1995.

Shewenn, R., Direct correlations between coronal transients and interplanetary shocks. *Space* Science *Reviews,* 34, 83, 1983.

Sheeley, N. R., R. A. Howard, M. J. Koomen, D. J. Michaels, R. Schwenn, K. H. Muhlhauser, and H. Rosenbauer, Association between coronal mass ejections and interplanetary shocks, *In Solar Wind Five,* M. Neugebauer, editor, NASA headquarters and the Jet Propulsion Laboratory, 1983.

Sheeley, N. R,, R. A. Howard, M. J. Koomen, I). J. Michaels, R. Schwcnn, K. H. Muhlhauser, and H. Rosenbauer, Coronal mass ejections and interplanetary shocks. *J. Geophys. Res.,* 90, 163-190, 1985.

Smith, E. J., and J. H. Wolfe, Observations of interaction regions and corotating shocks between one and five au. *Geophys. Res. Lett., 3,* 137-140, 1976.

Smith, E. J., and J. H. Wolfe, Pioneer 10, 11 observations of evolving solar wind streams and shocks beyond 1 au. *In Study of Traveling Interplanetary Phenomena/1977,* M. A. Shea, D.F. Smart, and S. T. Wu, editors, D. Reidel, 227-257, 1977.

Smith, E. J., Interplanetary shock phenomena beyond 1 au. *In Collisionless Shocks: Reviews of Current Research,* B.T. Tsurutani and R. G. Stone, editors, *Geophysical Monograph,* 35, 69,1985

Smith, E. J,, M. Neugebauer, A. Balogh, S. J. Bame, G. Erdos, R. J. Forsyth, B. E. Goldstein, J. I,. Phillips, and B. 1. Tsurutani, Disappearance of the heliospheric sector structure at Ulysses. *Geophys. Res. Lett., .20, 2327, 1993.*

Smith, E. J., A. Balogh, M.E. Burton, G. Erdos, and R. J. Forsyth, Results of the Ulysses fast latitude scan: magnetic field observations, *Geophys. Res. Lett., .23, 3325-3328,* 1995.

Wenzel, K. -P., R. G. Marsden, D. E. Page, and E. J. Smith, The Ulysses mission. *Astron.*

Astrophys. Suppl. Ser., 92, 207-219, 1992.

This manuscript was prepared with the AGU LaTeX macros v3.0.

Figure 1, Ulysses heliographic coordinates from its launch in October 1990 to the end of 1993. 'The Jupiter fly-by occurred in February 1992. The heliocentric range is in AU and the heliolatitude is in degrees, We divided this trajectory into six intervals (A, B, C, D, E, F) to analyze the shock waves and the large-scale structures in the solar wind.

Figure 2. Three hour averages of IMF magnitude and solar wind radial velocity during the in-ecliptic trajectory. This trajectory is divided into two intervals: Interval A, from 1 AU to 2.9 AU, characterized by transient activity; and Interval B, from 2.9 AU to 5.4 AU, dominated by interaction regions.

Figure 3. Large-scale IMF magnitude and solar wind radial velocity during the out-of-ecliptic trajectory. This trajectory is divided into four intervals (C, D, E and F). In July 1992 (interval D) we observed very high-speed solar wind coming from the south coronal hole. In May 93 (interval E) the disappearance of the magnetic sector structure produced dramatic changes in the shock population. At higher latitudes, interval F, the minimum of solar wind velocity rose causing the IMF magnitude to reveal fewer compressional events.

Figure 4. Map of large-scale events in the solar wind: in-ecliptic observations. Every 27-day row corresponds to an approximated Solar Rotation observed by Ulysses (SRU). SRU are numbered successively at the left-hand of the plot and the chronological order is from the bottom to the top, Denoted by characteristic symbols are shown: forward shocks (left arrows), reverse shocks (right arrows), ICMEs (blue), CIRs (red) and the background magnetic sector structure (positive= white, negative- gray).

Figure 5. Two interaction regions led by two forward shocks observed by Ulysses in 1991.

Figure 6. Map of large-scale events in the solar wind: out--of-ecliptic observations. The same format as the previous figure, but in this case the approximated Solar Rotations observed by Ulysses (SRU) correspond to 26 clays.

Figure 7. Duration (in days) of interaction regions against heliocentric distance as observed during the in-ecliptic trajectory. The interaction regions are divided into two types depending on the IMF polarity carried by the fast stream producing them. As expected, interaction regions increased their duration with heliocentric distance.

Figure 8. θ_{B_n} occurrence histograms for the three types of interplanetary shocks detected during the in-ecliptic trajectory (based on figure 4 and the shock list by *Balogh et al.* [1995a]). While most of the forward shocks (transient and corotating) were quasi-perpendicular (θ_{B_n} > 450), most of the corotating reverse shocks were quasi-parallel (θ_{B_n} < 450).

Figure 9. Heliocentric evolution of the Mach number of three types of interplanetary shock waves detected during the in-ecliptic trajectory. The N'lath numbers are from *Balogh et al. [1* 995a]. In March 1991 (interval A), we detected strong forward transient shocks associated with ICMES. In interval B, the strongest shocks were forward corotating shocks about 4-5 AU.

Figure 10. Duration of interaction regions detected after the Jupiter fly-by against south heliolatitude. The interaction region produced by the north coronal hole disappeared abruptly at about 17° south. interaction regions produced by the south coronal hole disappeared at about 38° south,

Figure 11. θ_{B_n} occurrence histograms for the four types of shock waves detected after the Jupiter fly-by (based on figure 6 and the shock list by *Balogh et al.*). In this case, forward corotating shocks and reverse corotating shocks seem about equally likely to be either quasi-parallel or quasi-perpendicular shocks.

Figure 12. Mach numbers (based on the shock list by *Balogh et al.*) against south heliolatitude for the four types of shock waves detected after the Jupiter fly-by. We detected very strong interplanetary shock waves (M_s > 3.5) between 10° and 20° south. Afterwards, forward shocks disappeared and reverse shocks tended to decrease their strength.

Figure 13. Two examples of transient reverse shocks detected by Ulysses after the Jupiter fly-by: a) on day 92:142, b) on day 93:085.

Figure 14. Percentages of the four types of shock waves detected by Ulysses in five intervals.

Table 1. Classification of interplanetary shock waves.

type of shock	characteristics
1. corotating shock	leading (CIR-forward) or trailing (CIR-reverse) an interaction region†
transient shock (not associated with an interaction region)	2. transient shock associated with an ICME‡
	3. transient shock no readily associated with an ICME

†The criteria to identify interaction regions is discussed in section 2.2.

‡The criteria to associate transient shocks and 1 CMES is discussed in section 2.5.

Table 2. ICMES, CIRS and interplanetary shock waves as detected in the six intervals. Interplanetary shocks (forward and reverse) are divided into t hree categories: *1)* CIR-shocks, *2)* transient shocks associated with ICME drvers, and *3)* transient shocks no readily associated with ICMEs (see table 1).

interval	ICMEs	CIRs	interplanetary shocks						
			cir-f	*cir-r*	f_t *icme*	r_t *icme*	f_t *unasso.*	r_t *unasso.*	*total*
A (sru 1- 7)	14	1	0	1	7	0	13	1	22
B (sru 8 -18)	11	18	20†	1 5	6	0	5	2	48
c (sru 19-23)	9	4	4	3	4	0	3	3	17
D (sru 24-34)	6	18	14	13	4	0	5	4	40
E (sru 35-41)	6	11	1	11	1‡	1‡	0	2	16
F* (sru *42-..)*	2	2	0	2	2‡	2‡	0	4	10

†Four CIRs were led by two forward shocks in this interval,

‡Transient shocks attributed to 'over-expanded' CMEs.

*Only the two first shocks of this interval are shown in figure 5.

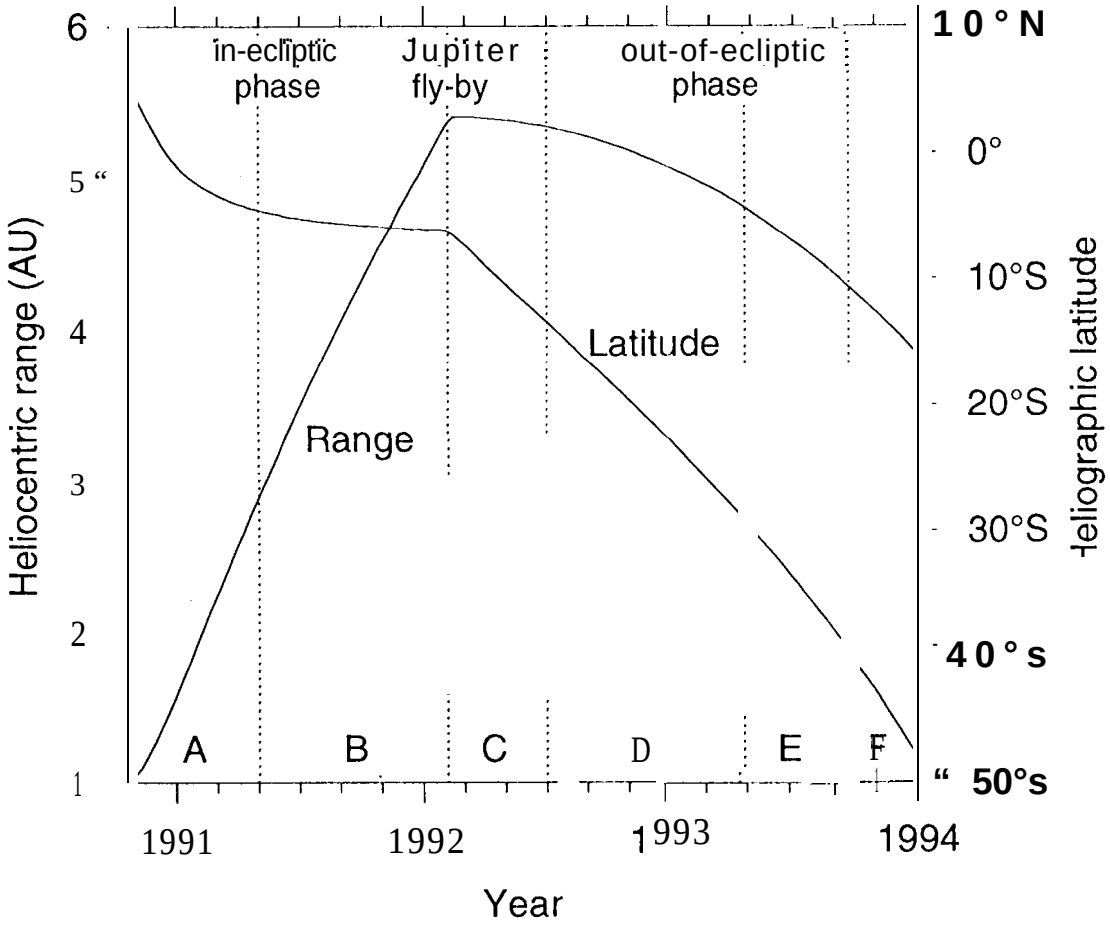

figure 1.

(Not for reproduction)

(Not for reproduction)

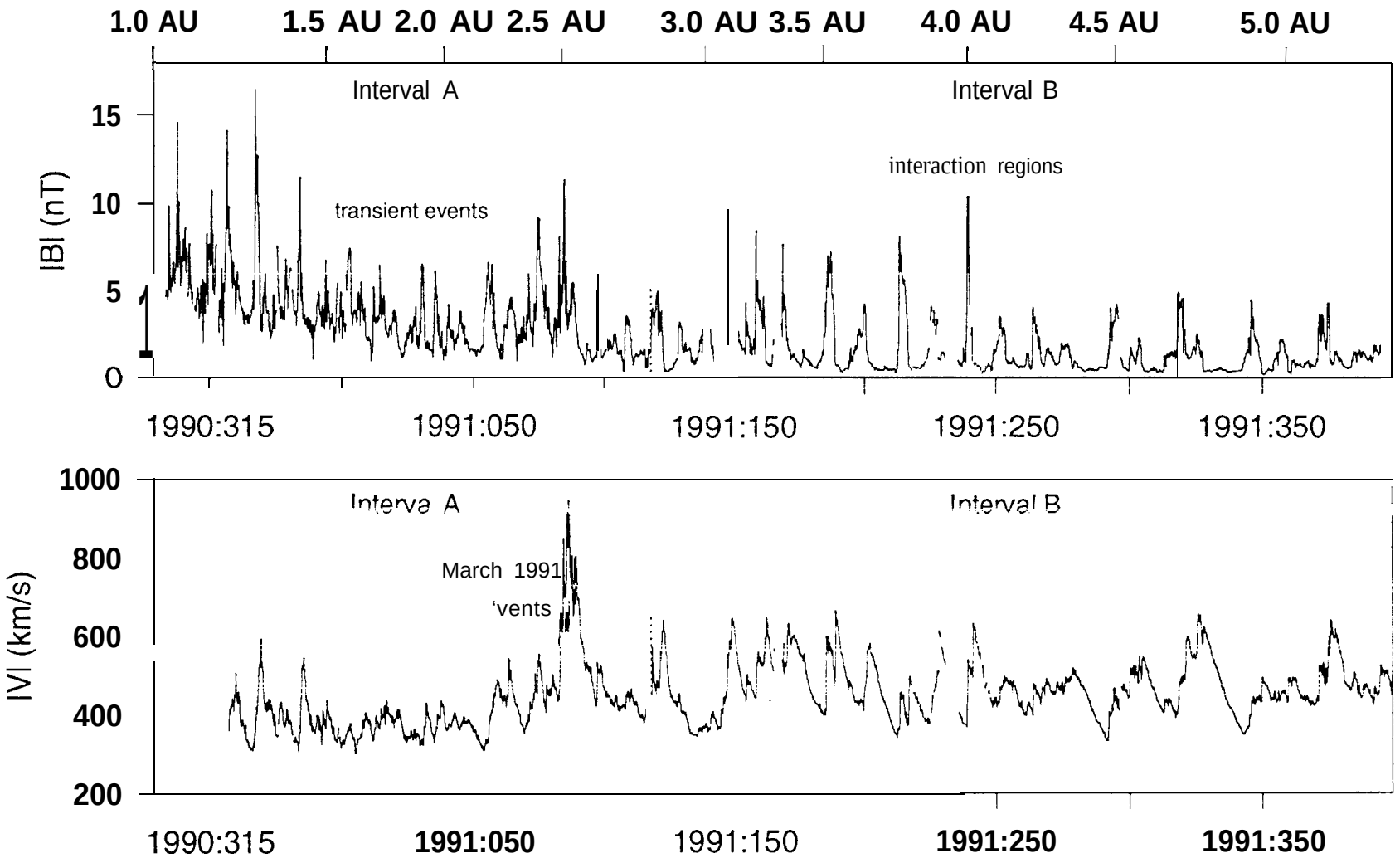

figure 2

(Not for reproduction)

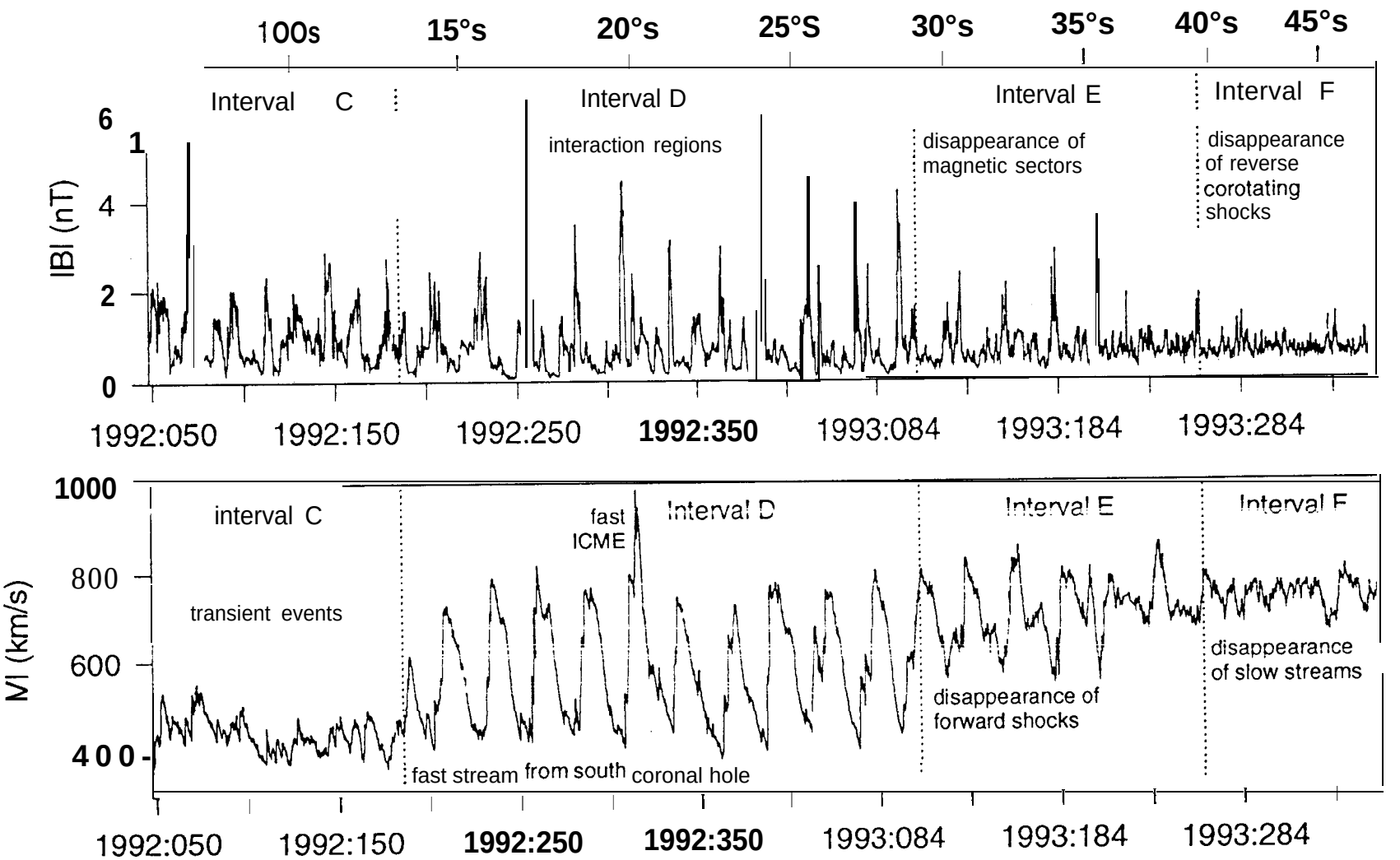

figure 3

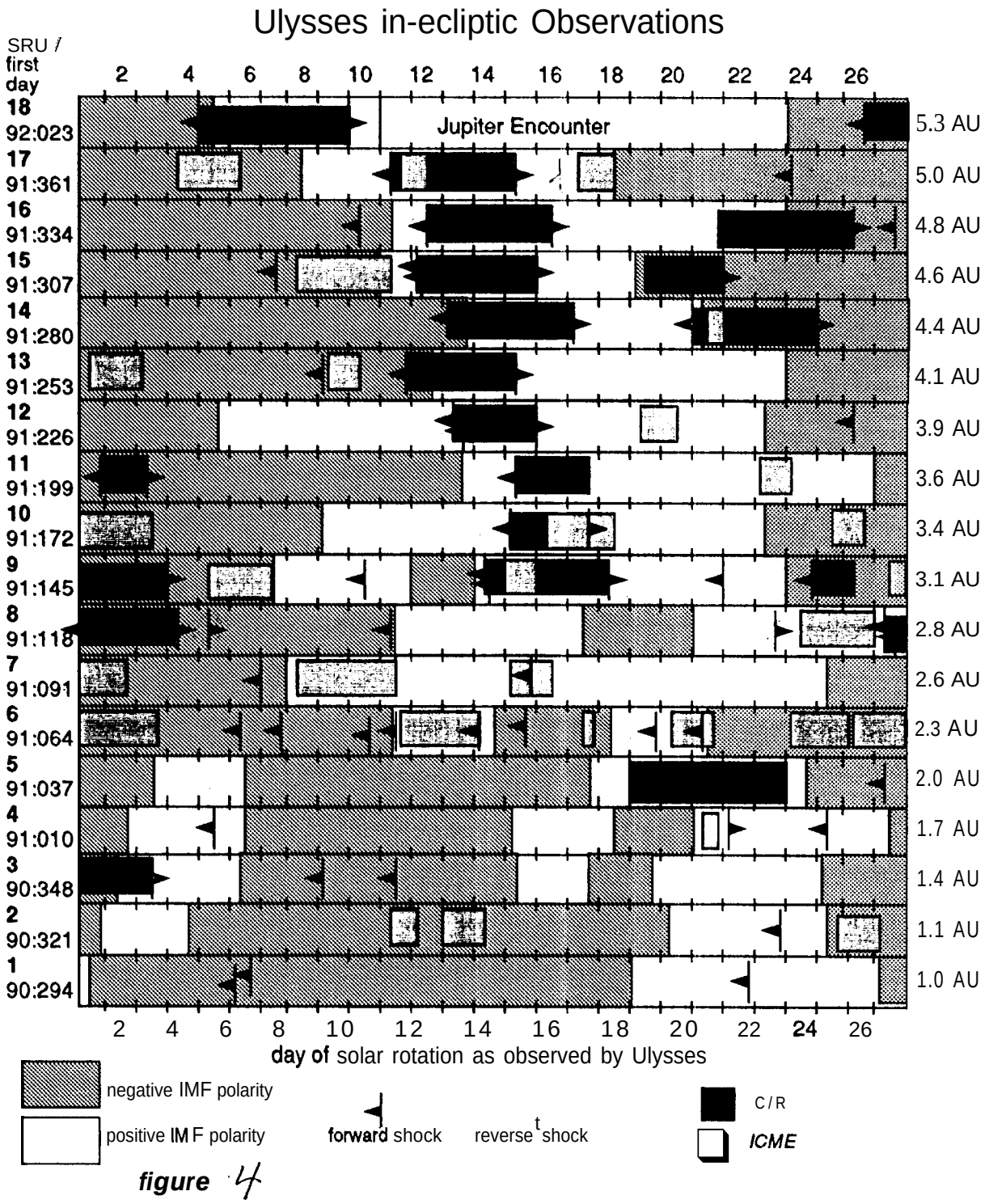
Ulysses in-ecliptic Observations
SRU / first day
2 4 6 8 10 12 14 16 18 20 22 24 26
18 92:023
17 91:361
16 91:334
15 91:307
14 91:280
13 91:253
12 91:226
11 91:199
10 91:172
9 91:145
8 91:118
7 91:091
6 91:064
5 91:037
4 91:010
3 90:348
2 90:321
1 90:294
Jupiter Encounter
5.3 AU
5.0 AU
4.8 AU
4.6 AU
4.4 AU
4.1 AU
3.9 AU
3.6 AU
3.4 AU
3.1 AU
2.8 AU
2.6 AU
2.3 AU
2.0 AU
1.7 AU
1.4 AU
1.1 AU
1.0 AU
day of solar rotation as observed by Ulysses
negative IMF polarity
positive IMF polarity
forward shock
reverse shock
C/R
ICME

figure 4

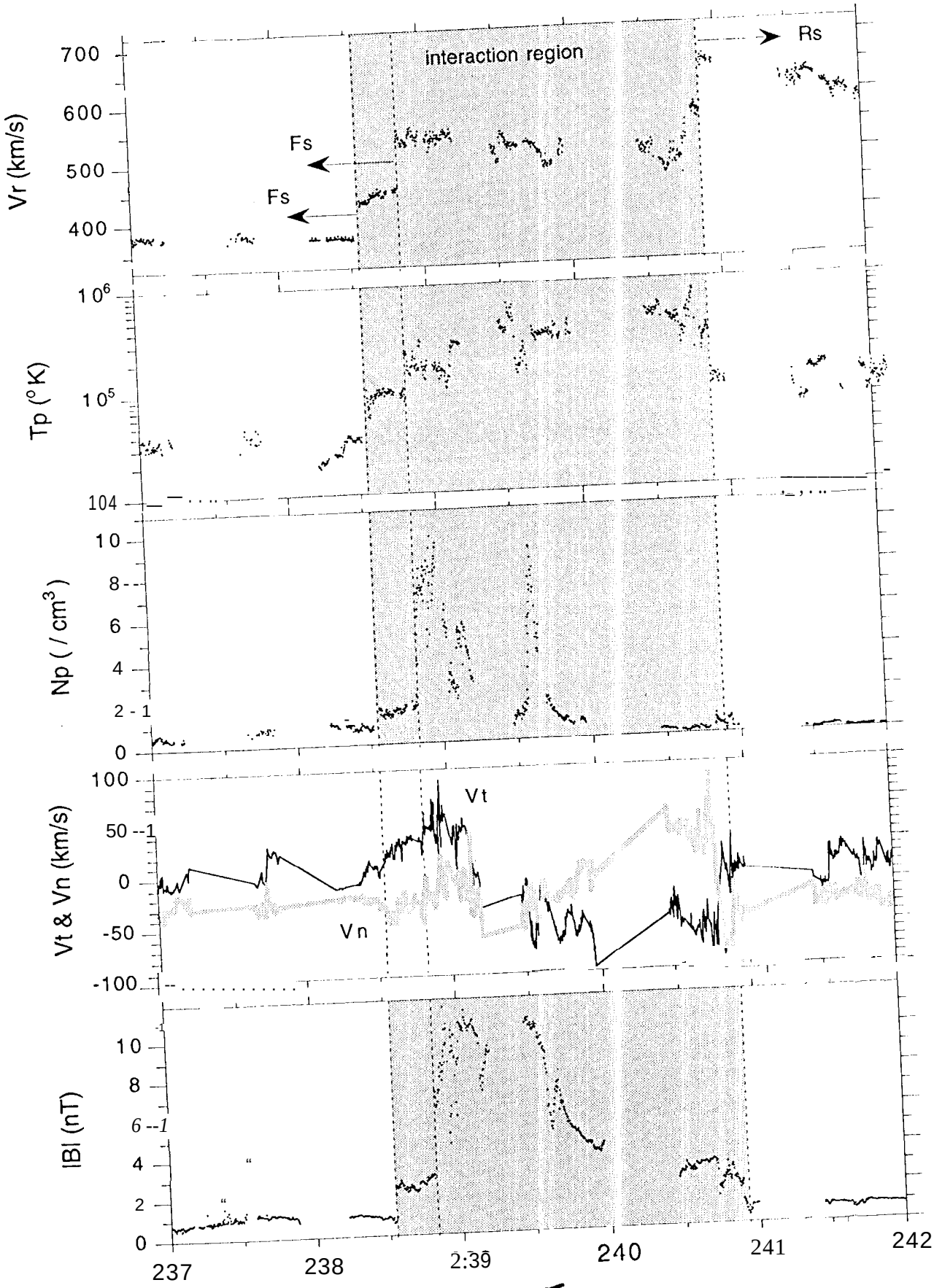

figure 5a
(Not for reproduction)

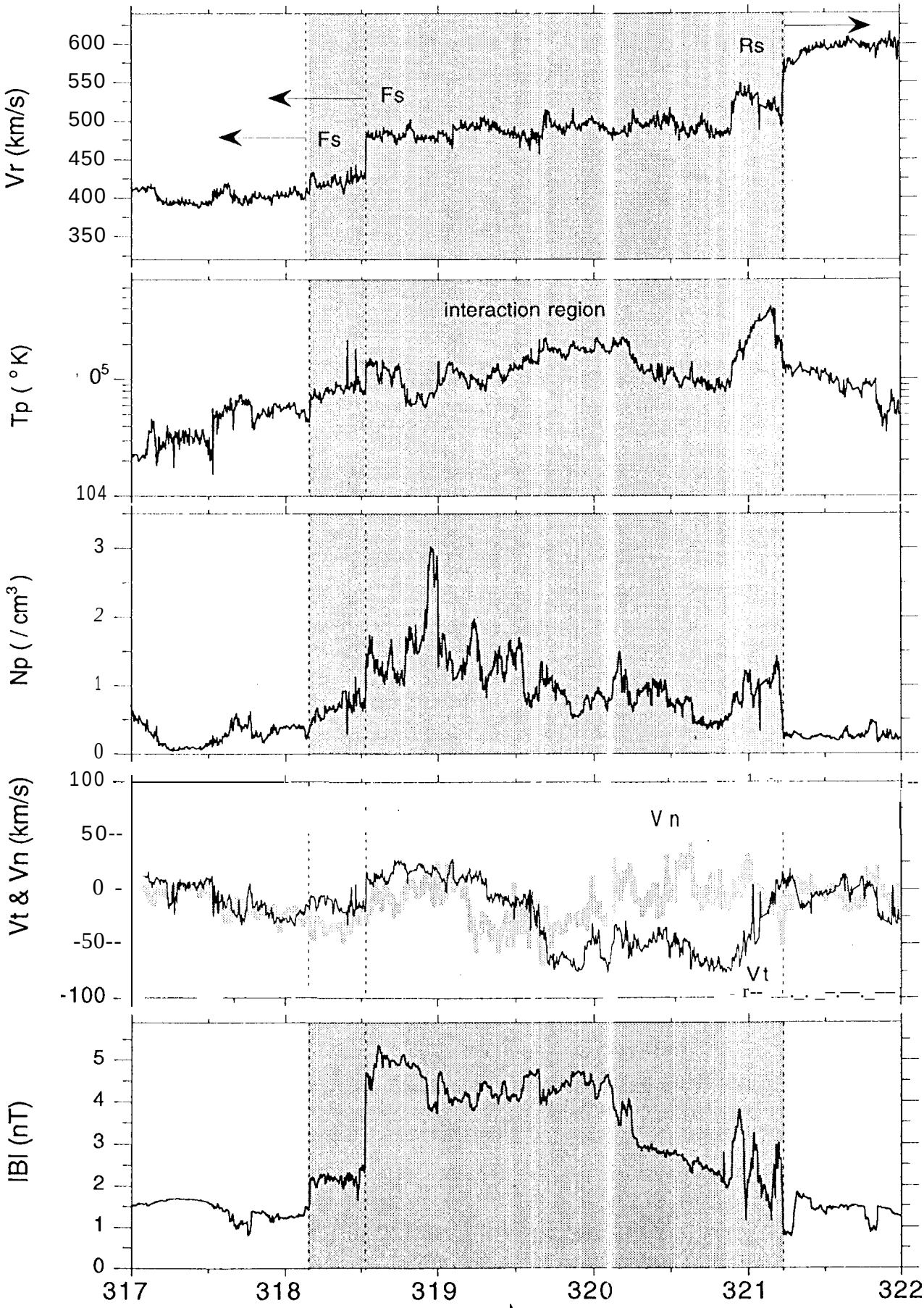

figure 5b

(Not for reproduction)

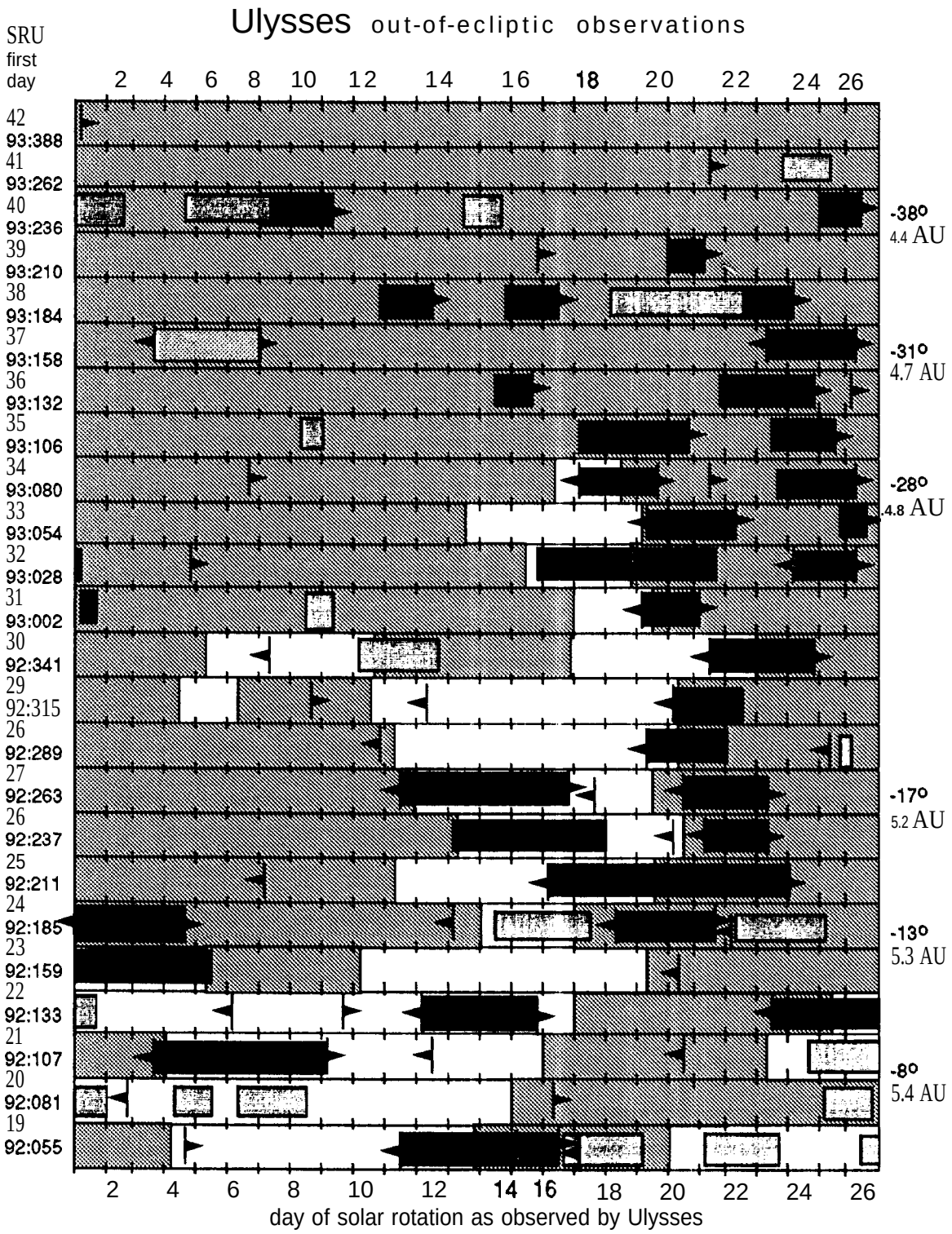
Ulysses out-of-ecliptic observations
SRU first day
2 4 6 8 10 12 14 16 18 20 22 24 26
42
93:388
41
93:262
40
93:236
39
93:210
38
93:184
37
93:158
36
93:132
35
93:106
34
93:080
33
93:054
32
93:028
31
93:002
30
92:341
29
92:315
26
92:289
27
92:263
26
92:237
25
92:211
24
92:185
23
92:159
22
92:133
21
92:107
20
92:081
19
92:055
-38°
4.4 AU
-31°
4.7 AU
-28°
4.8 AU
-17°
5.2 AU
-13°
5.3 AU
-8°
5.4 AU
2 4 6 8 10 12 14 16 18 20 22 24 26
day of solar rotation as observed by Ulysses

figure 6

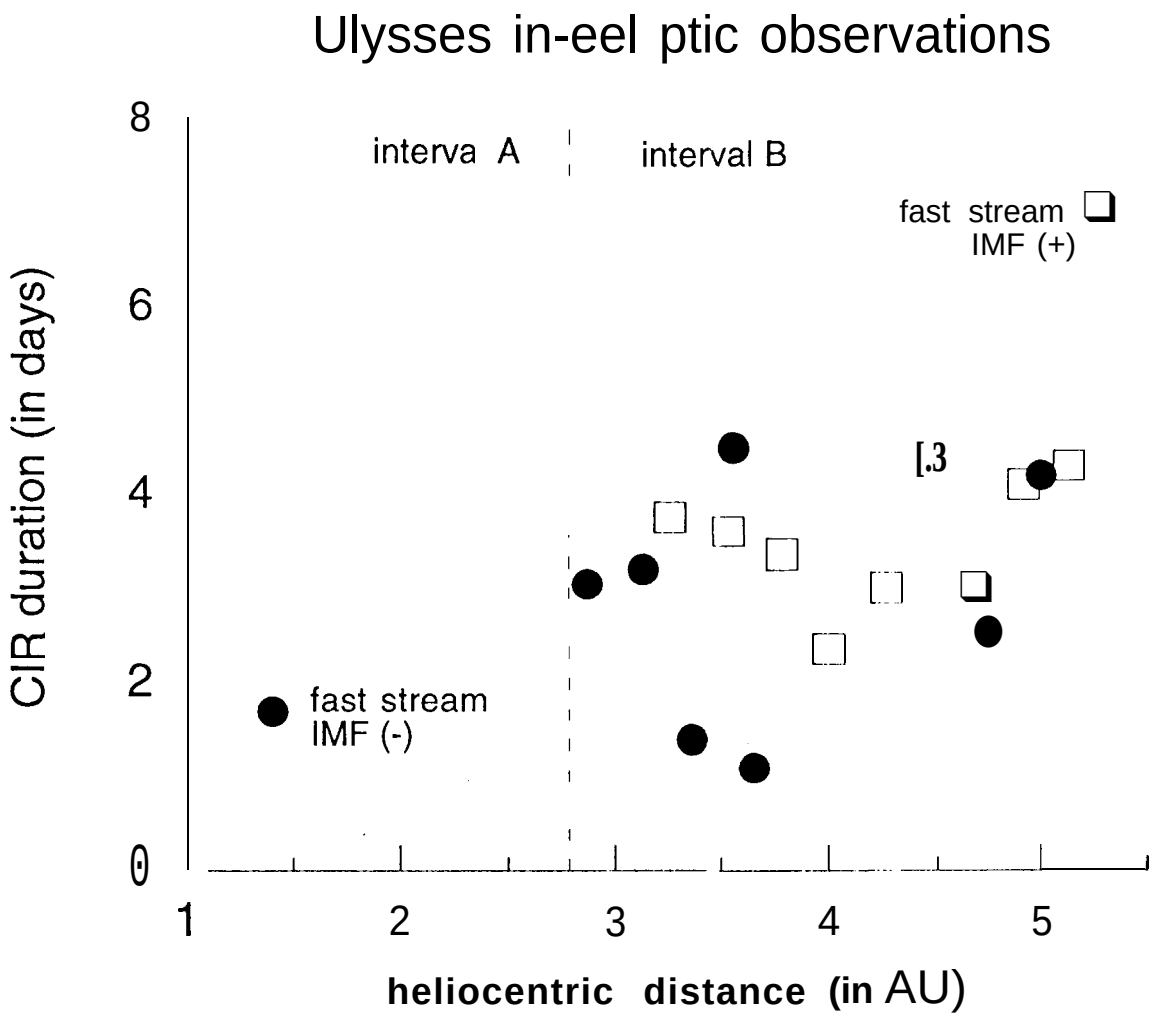

figure 7

(Not for reproduction)

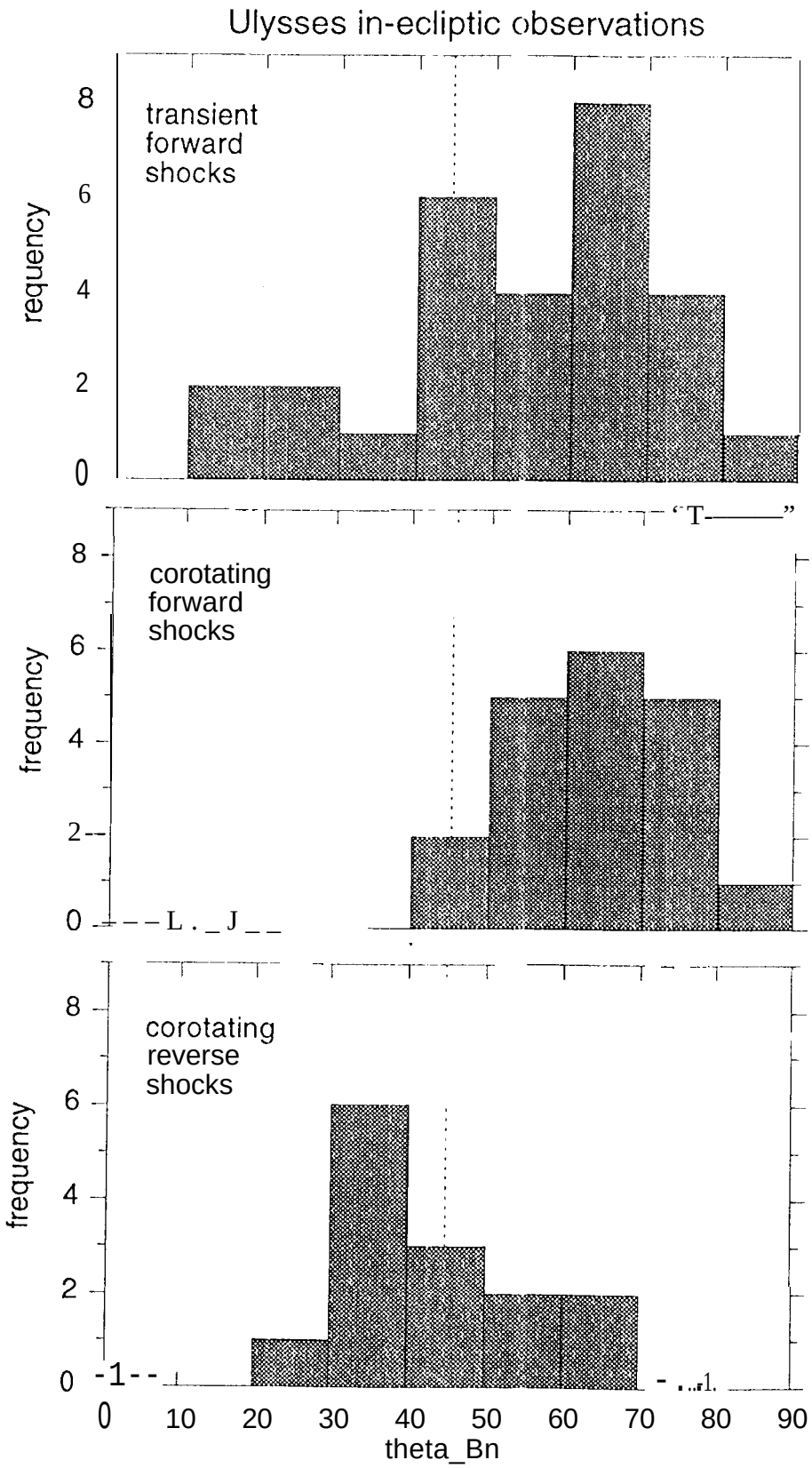

(Not for reproduction)

figure 8

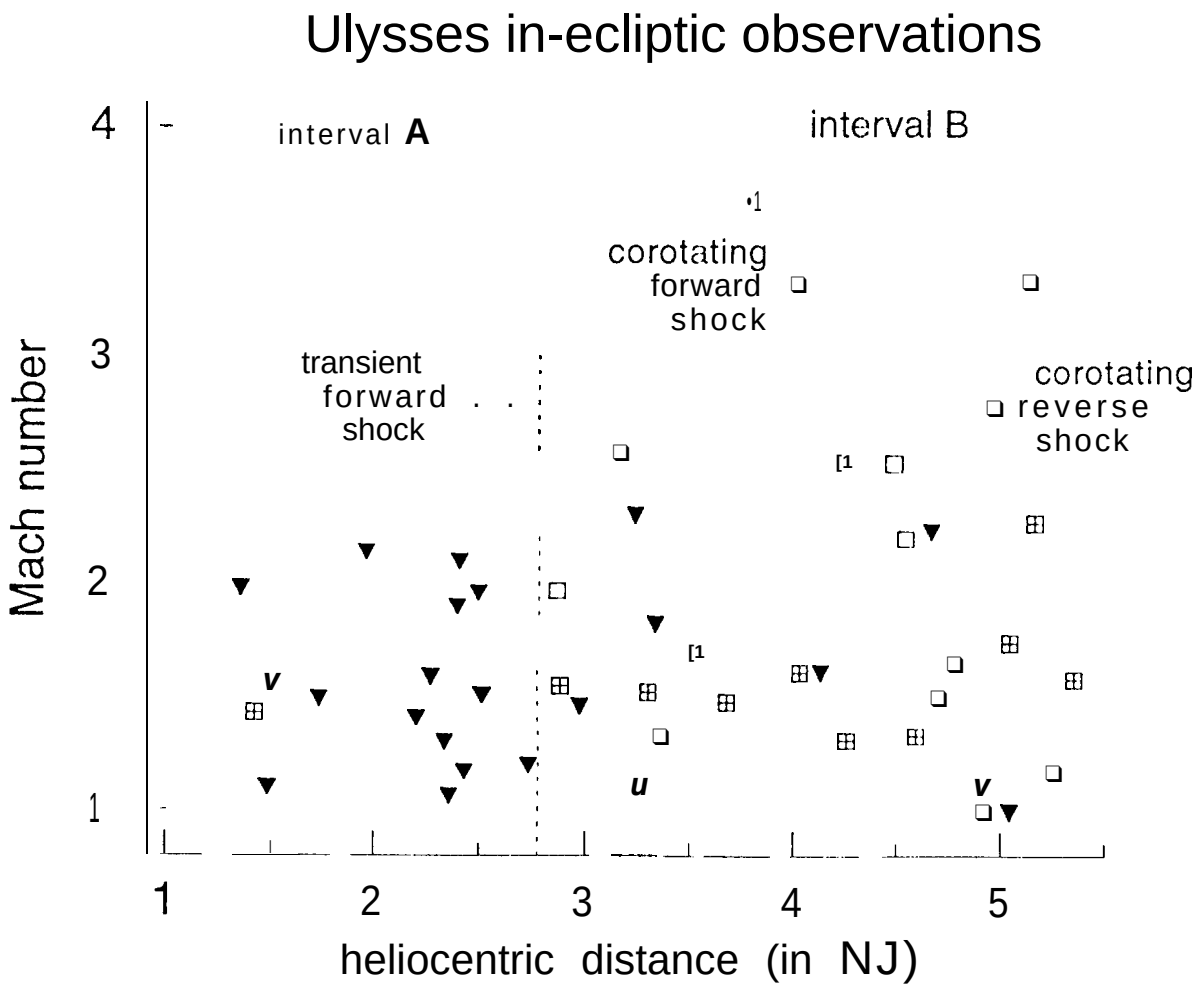

(Not for reproduction)

figure 9

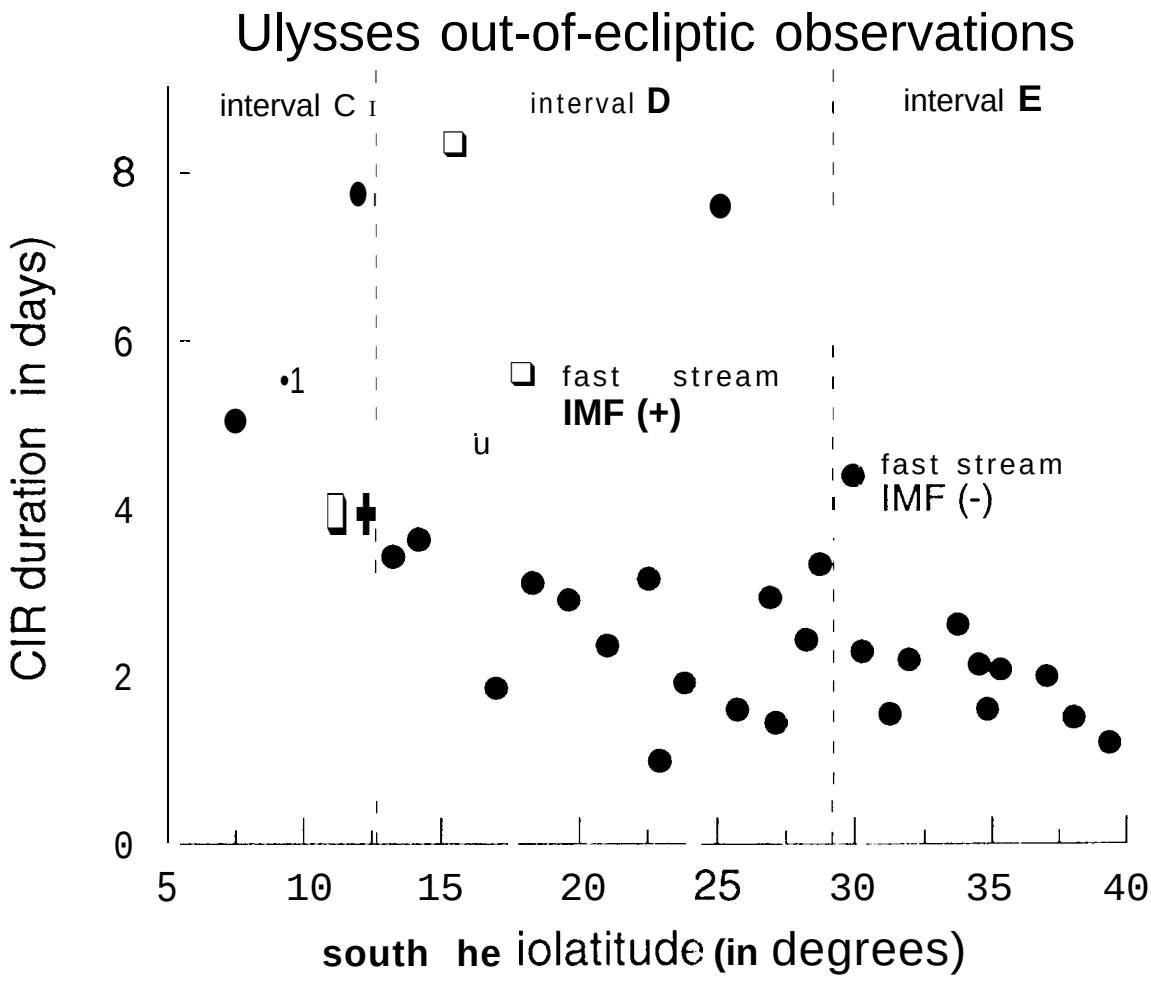

figure 10

(Not for reproduction)

Ulysses out-of-ecliptic observations

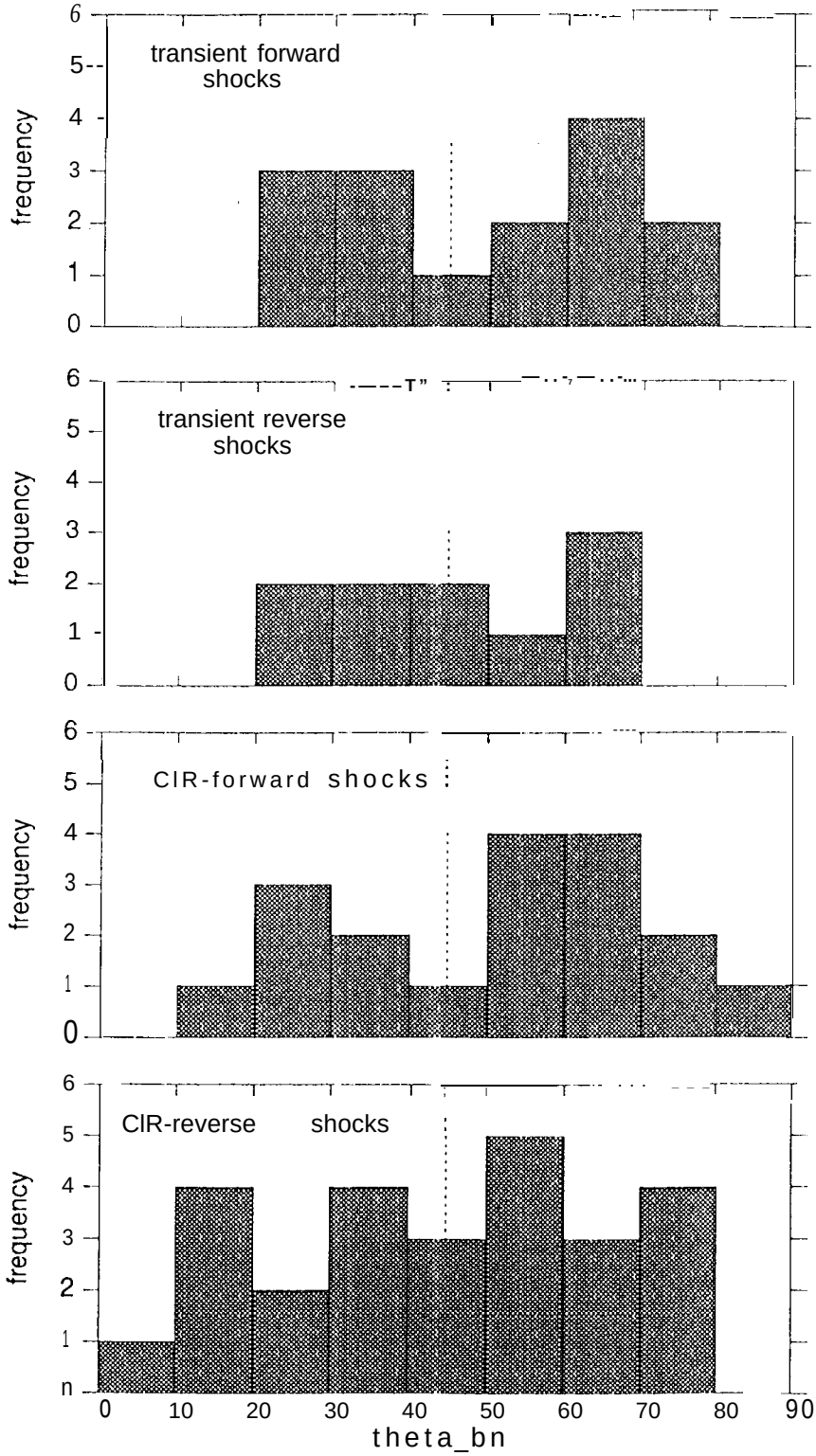

(Not for reproduction)

figure 11

Ulysses out-of-ecliptic shock observations

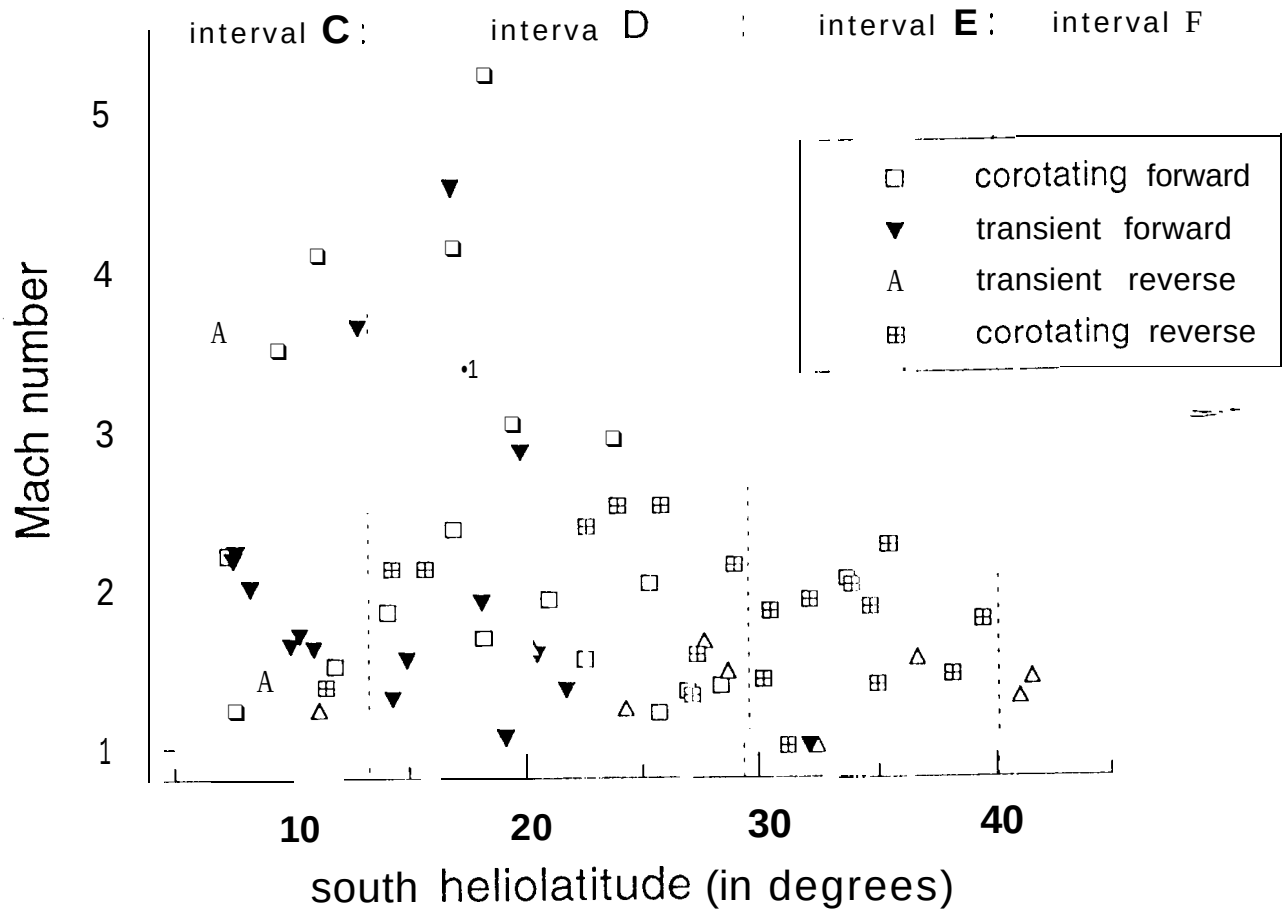

(Not for reproduction)

figure 12

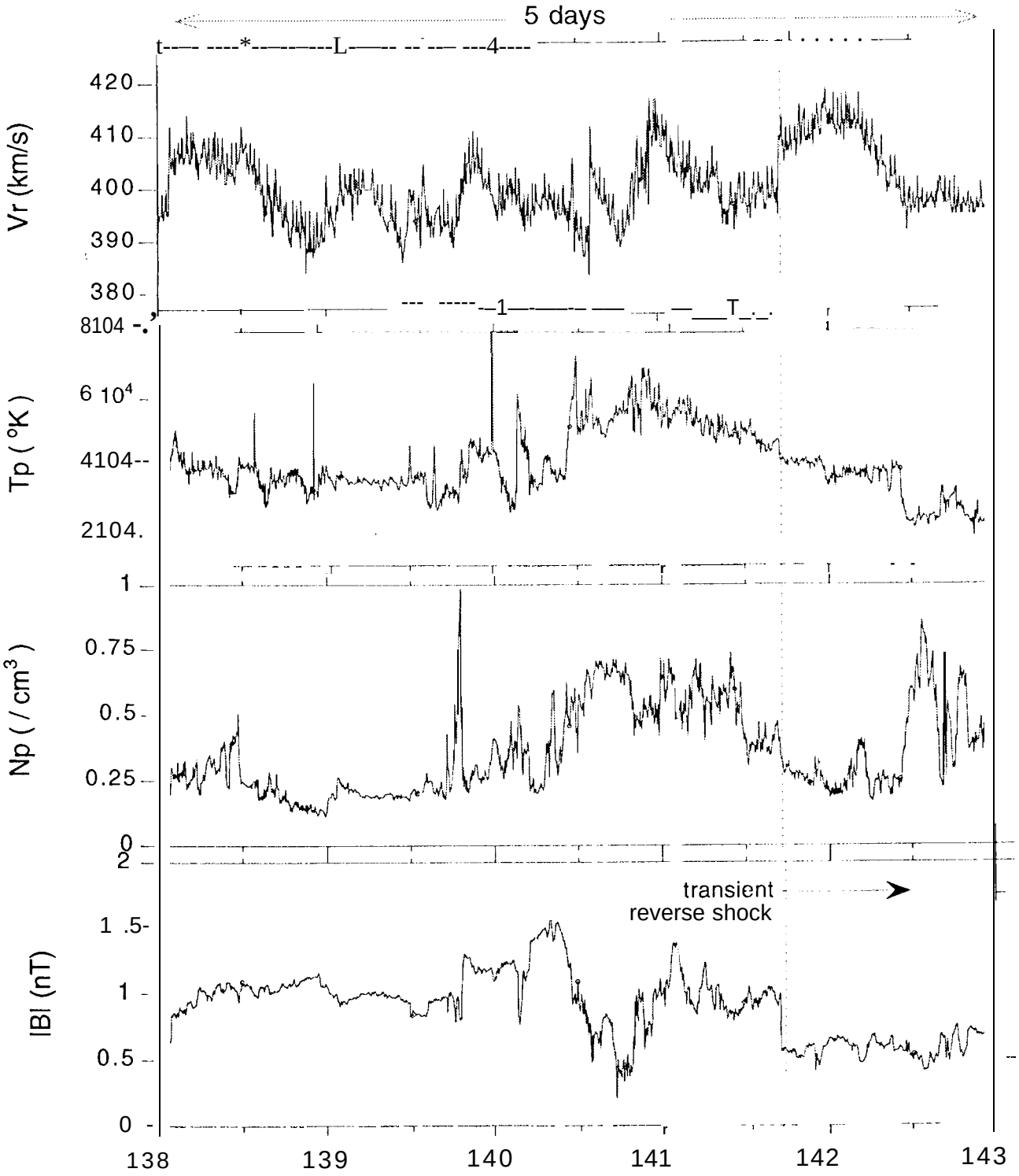

figure 13a

(Not for reproduction)

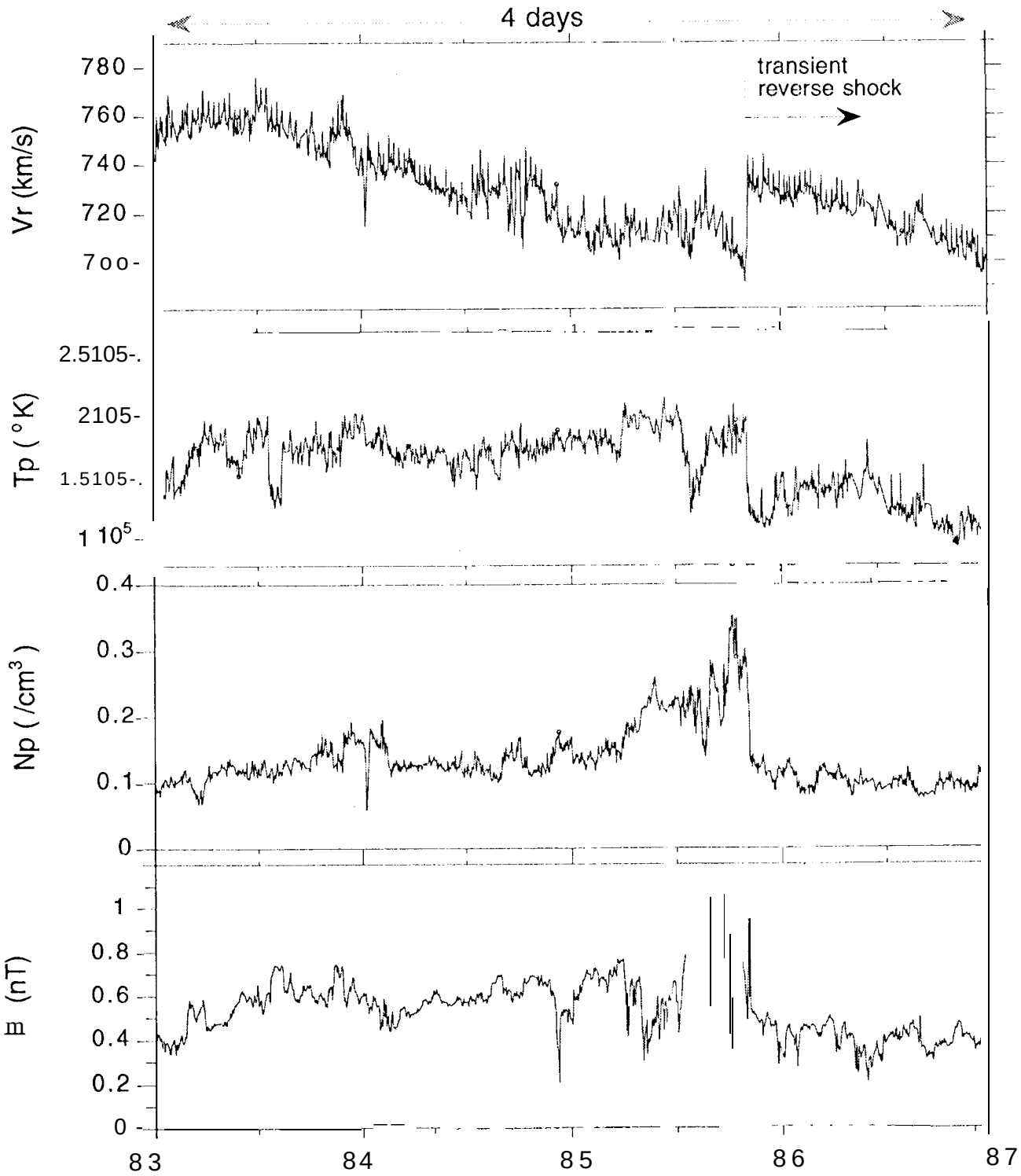

figure 13b

(Not for reproduction)

shock populations in five intervals: Ulysses

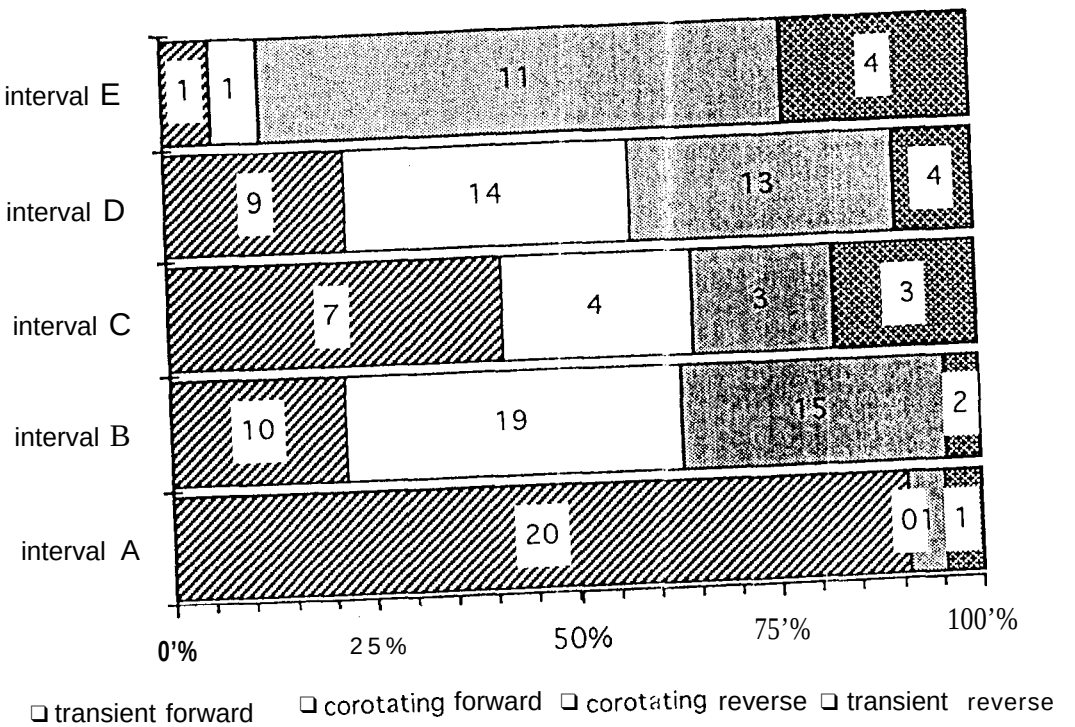

figure 14

(Not for reproduction)

Slices: A Scalable Concurrent Partitioner for Unstructured Finite Element Meshes

Hong Q. Ding and Robert D. Ferraro
Jet Propulsion Laboratory, MS 169-315, Pasadena, CA 91109

A concurrent partitioned for partitioning unstructured finite element meshes on distributed memory architectures is developed. The partitioned uses an element-based partitioning strategy. Its main advantage over the more conventional node-based partitioning strategy is its modular programing approach to develop parallel applications. The partitioned first partitions element centroids using a recursive inertial bisection algorithm. 1 :lements and nodes then migrate according to the partitioned centroids, using a data request communication template for unpredictable incoming messages. Our scalable implement ation is contrasted to a non-scalable implementation which is straight forward parallelization of the sequential partitioner. The algorithms adopted in the partitioned scales logarithmically, as confirmed by actual timing measurements on Intel Delta onupto512 processors for scaled size problems.

1 Introduction

Finite element analysis is used in broad and diverse areas, such as structural analysis in mechanics, fluid dynamics, electro-magnetics etc. Ever-increasingly larger and complex mesh geometries used in practical applications can only be dealt with the distributed memory parallel supercomputers because of their ability to scale to large number of processor without losing reasonable performance.

Partitioning a finite element mesh among the processors of a parallel supercomputer sets up the stage for the finite element analysis problem. The domain partition achieves load balance, preserves proper data locality and reduces communications during the solution of the problem.

Partitioning algorithms, especially for simple grids, has been studied in considerable details (see [1,2] for summaries of recent related works). Most of these work study the grid mesh problems and the number of edges being cut by the processor subdomain boundary is used as the measure of quality of the partitioned. However, partitioning a finite element mesh involves additional complexities due to presence of the elements.

2 Node-based partitioning strategy

In a node-based partitioning strategy, one simply partitions the nodes (grids on the mesh that forms the elements). Therefore, each node belongs uniquely to a processor. Elements are then assigned to the nodes. Some elements will not be uniquely assigned because they have nodes which reside in different processors. If we simply assign one such element to one of the relevant processors, that element has to remember that it has some nodes residing on other processors. This causes inconvenience, because in finite element analysis, many computations are done based on the elements, not the nodes. For these elements which have nodes on other processors, computations have to be carefully designed to get relevant nodal i nforrnation fi om other processors, therefore rewriting the relevant part of the sequential codes. If further adaptive refinement is required, nodes on other processors must be brought in so that all elements on the processor have all their nodes 1 ocall y available before further refinements can proceed. Notice here that the number of edges

being cut directly relates to the number of nodes needed to be brought in for element related calculations. This partitioning strategy has been used in [3].

3 Element-basc(l partitioning strategy

Because the finite elements analysis are fundamentally element based, we prefer an element-based partition where an element in its entirety belongs to a processor uniquely. This implies that all the nodes of an element must be on this processor too. We partition the finite element mesh by associating each element to its center of mass (centroid) and partitioning the resulting collection of centroids via a recursive inertial bisection algorithm. Once the elements are partitioned, nodes are migrated to the processor where their related elements are. Now, processor subdomain boundaries go along the edges, instead of cut across the edges in a node-based partitioning. A node on processor subdomain boundaries is replicated on all processors which share it. A brief description of the element-based partitioned has been previously published in [4].

The most important feature of this partitioning strategy is that the local mesh resulted from the partitioned is complete simply connected mesh, and all element-based calculations proceed as in sequential case, without reference to any non-local information. As a result, most of those complicated sequential finite element analysis codes can be used without change. Further local adaptive refinements and multi-level solution methods could be also applied easily because all relevant information is locally available. Some of the boundary nodes of the local mesh are true boundary nodes subject to boundary conditions. Other boundary nodes are actually interior nodes, but on the processor subdomain boundaries. The finite analysis treat these processor boundary nodes simply as interior nodes, no different from other interior nodes. It is the parallel solvers which connects the local meshes into a global mesh and constructs the global stiffness equation and solves it[5]. This separation allows people in the application area concentrate on the finite clement analysis and the solver being independently developed by people in the parallel algorithm area. This achieves much better modularity, and it is much easier to complement compared with the above node-based partitioning strategy.

In the following, we describe more details of our element-based concurrent partitioned which contains two major stages. First, the centroids are partitioned. Second, nodes and elements migrate according to centroids. We emphasize that algorithms used in both stages are scalable, i.e., no worse than a logarithmic scaling. Finally we present several example applications and the timing measurements.

4 Recursive Inertial Bisection

The collection of centroids of elements form a mesh dual to the original node mesh. Partitioning of the centroids proceeds exactly as partitioning of grids. The edges in the centroid mesh does not correspond directly to anything in the original node mesh, but the cut of an edge in the centroid mesh directly corresponds to an edge in the original node mesh. Therefore, the number of edges being cut during the recursive partitioning of the centroid mesh equals to the number of edges on the boundaries of the partitioned node meshes.

Although recursive spectral bisection is generally considered to give the best partitions, its parallel implementation involves solving large eigen-value eigen-vector problems which is difficult to implement efficiently on parallel computers. Recursive inertial bisection (RIB) usually leads to reasonable partitions with reasonable aspect ratio, because in each recursive step, the remaining mesh subdomain is always cut into two across its current longest extension; thus avoids long and thin subdomains often occurring in the standard

recursive coordinate bisection. RIB can be implemented in parallel with high efficiency, Our partitioned uses the RIB algorithm.

Theoretically the RIB algorithm completes in $\log_2(P)$ recursive steps, where P is the desired number of partitions which is equal to the number of processors. However, $\log_2(P)$ steps does not imply a CPU time proportional to $\log_2(P)$, given the total problem size fixed. First, let us look at the basic steps in the RIB algorithm. A brief description follows. Each centroid has a flag indicating which region it belongs to. In the first step, there is only one region and all centroids belong to this region. We wish to divide this region into two. The inertial tensor is calculated, diagonalized, and the principle axis (which points to the longest extension) is found. All centroids are projected onto this axis, which forms an one-dimensional array of float point numbers. The median value of this array of numbers is calculated. Depending on whether its projection is lower or higher than the median, each centroid knows which of the two regions it belongs to. In the second recursive step, this process is repeated on the two regions independently to produce 4 regions. In the third recursive step, the 4 regions are divided into 8 regions. And finally, in the $\log_2(P)$-th recursive step, P/2 regions are divided into P regions. From this description, we see that there are $1+2+4+ \ldots + \frac{P}{2} = P - 1$ regions being calculated during the $\log_2(P)$ recursive steps, although the number of points in each region is reduced by half in each recursive step.

4.1 Non-scalable implementation

A straightforward conversion of the above sequential RIB algorithm to a parallel partitioned is not scalable. In that implementation[6], at beginning, nodes and elements are read in from disk and are distributed in some fashion. The above basic RIB steps are performed without moving any data around. Only at the end nodes and elements migrate to their final destination processor (or processors) according to the region flag. All the calculations of element centroids, the region inertial tensor, eigenvector and median finding are carried out in a synchronously way, such that every processor participated in all the calculations, with zeroes padded in as necessary similar to operations in a SIMD machine like CM-2. The net effect is that each processor does work proportional to P .

4.2 Scalable implementation

A scalable implementation uses processor group concept, a feature nice] y supported by Message Passing.interface (M PI) standards (although we have written a library[7] to implement partial operations on groups of processors in the Intel Paragon NX environment). Here, once the entire centroids mesh are divided in two regions, the centroids physically moves to the relevant processors. For example on 64 processors, all centroids with projection smaller than median goes to processors 0-31, and all other centroids to processors 32-63. In the next recursive step, two partitioning process proceed independently on the two processor groups to produce 4 subdomains on 4 processor groups. This process repeats until we have 64 subdomains on 64 processors.

In this implementation, each processor does $\log_2(P)$ calculations of region inertial tensor, eigenvector, and median finding calculations. Although this is still more than the theoretical limit of $(P-1)/P$. 1 , it grows much slower than the linear scaling in the above non-scalable implementation.

5 Migration

In the node-based partition strategy, once the nodes are partitioned, elements need to be migrated according to the partitioned nodes. When the relevant nodes of an element are dis-

tributed on different processors, a decision has to be made as which processor to migrate the element to.

In the element-based partition strategy, once the elements are partitioned, only nodes have to migrate accordingly. In our element-based partition, nodes on subdomain boundaries are identified and replicated on relevant processors. A list containing these relevant processors' ids is replicated together with the node itself.

Our implementation of the element-based partition involves an extra stage, which simplifies the coding effects. In principle we can let the elements go together with the centroids during the recursive bisection process, so that when recursive bisection finishes, elements are in the right processors. However, elements are heavy --- they contains much information beyond the simple coordinates, thus put extra burden during the moves cross the network in the recursive bisection. We prefer to move these heavy elements only once in the extra element migration stage. Another reason for migrating elements after centroids are partitioned is that an element has to inform its nodes which processors to migrate to. If the element leaves the processor where its nodes reside, it has to have a mechanism to know which processor these nodes are and send relevant information to this processor. These extra complexities are all absent if the element remains in the processor during the recursive partitioning of the element centroids and then migrate after it has informed its nodes about their destination processors.

Among the identically replicated nodes, only one is considered the original node owned by a processor, and others are considered copies of the original node. not owned by the processor. This ownership is important for later solution of the stiffness equation, where only the owned nodes has corresponding component. Load-balance on solving the stiffness equation is largely proportional to the number of components each processor has. Note that an element-based partition ensures only that number of elements on each processor are same, but the number of nodes on each processor is not necessarily the same. Since only owned nodes counts in load-balance considerations in the solution phase, we can change the load-balance by reassigning node ownership. For example, node 108 is replicated on processors 1, 5,23,54, and is owned by processor 5. It may occur that processor 5 has more owned nodes than other processors. So we can change the ownership to 23 assuming processor 23 has less owned nodes than other processors. A fast stochastic algorithm is implemented to balance the owned nodes to about 3% load-imbalance in 5 iterations on 64 processors.

6 Template for Unpredictable incoming Messages

A data request protocol frequently occurs in the migration of elements and nodes. For example, the already partitioned centroids request that the element structures migrate to the processor where the centroid structures are. The requesting processor know which processor to send requests, but the receiving processor does not know how many messages it should expect and how long each message is? This is a problem of unpredictable incoming messages.

We designed a scalable (no worse than the logarithm of number of processors) communication template to resolve this problem as the following; (a) sort data requests on sending processor accoı ding to the destinations, (b) call two global communication routines global-sum() and global-maximum() so that each receiving processor knows how many messages it should expect and the maximum message length; (c) make correct number of cal 1s to receive the requests with the maximum message length it expects.

Once data requests are received, each processor send the requested data back to the requesting

processors. Elements and nodes migration are implemented using this communication template. Minor modifications to the template codes are made to handle the complications due to the variable number of nodes each finite element could have and due to the variable number of processors that a node is shared.

7 Further Adaptive Mesh Refinement

As explained above, a local mesh on a processor resulted from our element-based partition is a complete mesh with all elements and nodes geometric information locally available. One can therefore apply a sequential refiner to adaptively refine the local mesh independently. (This sequential adaptive refining program is specific to a user, therefore outside this partitioned package. It is to be supplied by the user.) An algorithm exists (written by J.Z. Lou at JPL) to match the newly created nodes along the subdomain boundary, thus connecting all local meshes into a global one. After the adaptive mesh refinements, another round of mesh partitioning is required to balance the loads.

This round of partitioning differs from the first round of partitioining in that this time the nodes are replicated, whereas in first round the nodes are not replicated. Complications arise here because in order to avoid ambiguities, only owned nodes should be replicated according to the newly partitioned elements. Non-owned nodes are still needed when elements inform its nodes their final destination. Afterwards, processor lists are constructed for every nodes, both owned and non-owned. Then non-owned nodes send processor lists to owned nodes. Owned nodes combine, sort and squeeze these processor lists to produce a final processor list and replicate themselves. Our concurrent partitioned has this process built-in.

8 Connection to a Sparse Solvers Package

The stiffness linear equations arising from finite element analysis is usually very large and sparse; its solution on a parallel architecture is also a main consideration. Fortunately, as discussed above, the local sparse coefficient matrix construction based on the resulting local mesh partitions from our element-based partitioned is a straightforward sequential process, which can be done by the user with their existing sequential codes, calculating contributions of finite elements to varies entries in the local sparse matrix.

The task of integrating local sparse matrices into the global sparse matrix (in fact, interpreting them as appropriate matrix blocks in the global matrix) and solving the global equation can be carried out by invoking an existing sparse matrix parallel solvers package[5] that we have developed in connection with the partitioned. The solver suit deals with symmetric complex in-definite matrix problems. A preconditioned hi-conjugate gradient method, a two-stage Choleksy factorization method, and a hybrid method combining both methods have been implemented. All three solvers uses a unified data interface so that users can switch to anyone of them at link time. This is quite convenient for those problems which is not positive definite. Furthermore, the local sparse matrix construction based on the local mesh partitions produced in our partitioned is well defined and is therefore standardized into subroutine calls in the solvers package. Thus the user does not need to worry about the sparse matrix organization at all. The user concentrates on the physics problem itself and calculates matrix entries and make subroutine calls to put them in place. We emphasize that this modular programing approach to parallel computing is make possible by our element-based mesh partitioning strategy. For more details, see [5].

9 Performance Characters

We measured two performance characters of the concurrent partitioned on Intel Delta with up to 512 processors. The data is either a 32768 hexagon elements mesh (squares in Fig. 1) or a 24264 tetrahedron elements sphere-cylinder (circles in Fig. 1). The fixed-size-performance is shown in Figure 1. In the region from small to medium number of processors (up to 128 processors), the total time reduces as the number of partitions increases. However, as the number of processors becomes larger than 128 (i.e., the resulting number of partitions becomes larger than 128), timing becomes flat or slight increase.

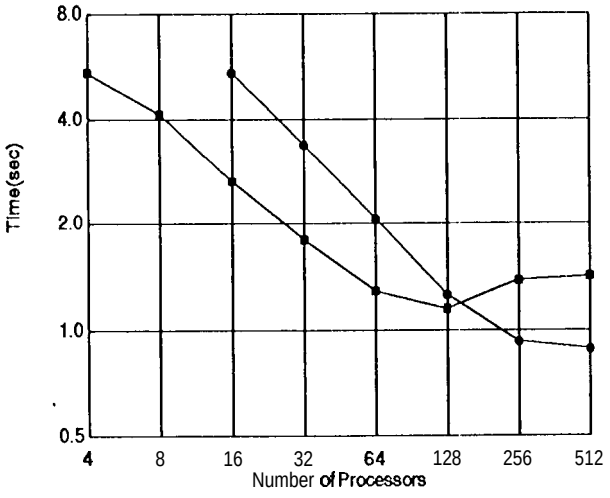

Fig.2 Execution time for two problems with fixed sires

The scaled size scaling behavior on increasing the problem size in proportion to the number of processors are also studied (see Figure 2). On 4-processor, the partitioned takes 0.21 sec to partition the 512 element problem (each element is 8-node hexagon). The 4096-element problem on 32-processor takes 0.51 sec. while the 32768-element problem on 256-processor takes 0.93 sec. If we take 4-processor as the minimum processor size where a partition algorithm make sense and normalize all timing accordingly, a logarithmic scaling is clearly followed for this scaled size pı oblem:

$$T(P)/T(4) = 0.8 \log_2 (P/4)$$

for P processors. This indicates the scalable nature of the many algorithms implemented in the partitioned.In comparison, an earlier non-scalable implementation results are also shown in Fig.2 as the top curve.

It should be emphasized that the absolute wall clock time here is very short, typically about a few seconds to half minute (excluding IO, as in most performance measurements).

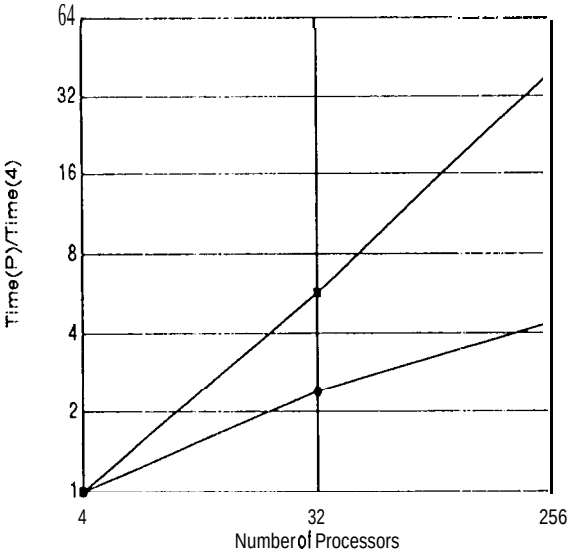

Fig.3 Execution time for a scaled size problem. 128 hexagon elements per processor

10 Summary

We have developed a concurrent partitioned for partitioning unstructured finite element meshes on

distributed memory architectures using an element-based partitioning stragety. We explained in details the scalable implementation of the recursive inertial bisection algorithm. Issues in migrating nodes and elements are discussed. Test runs of our paritioner on large meshes indicates a logarithmic scaling for increasingly larger problem size on larger number of processors, thus demonstrating the scalability of the algorithms implemented in this partitioned. Finally, we emphasized the modular programing approach to separate application specific sequential parts from the parallelization related algorithmic parts so that users can concentrate on their application, whereas the complications due to parallelization are handled by software developers.

Acknowledgement

We thank Jim McComb for explaining details of an old implementation [6]. We thank Concurrent Supercomputing Consortium for the use of Intel Delta. This work is carried out at Jet Propulsion Laboratory, California Institute of Technology, under a contract with National Aeronautics and Space Administration.

References

1. S. T. Barnard, A. Pothen, and H. D. Simon, A Spectral Algorithm for Envelope Reduction of Sparse Matrices, in Proceedings of Supercomputing 93, IEEE Computer Society Press, Los Alamitos, CA. p.493.

2. R. Leland and B. Hendrickson, An Empirical Study of Static Load Balancing Algorithms, Proceedings of Scalable High Performance Computing Conference, 1994, IEEE Computer Society Press, Los Alamitos, CA. p 682.

3. M.T. Jones and P.E. Plassmann, Parallel Algorithms for Adaptive Refinement and Partitioning of Unstructured Meshes, Proceedings of Scalable High Performance Computing Conference, 1994, IEEE Computer Society Press, Los Alamitos, CA. p 478.

4. H.Q. Ding and R.D. Ferraro, Slices: A Scalable Partitioned for Finite Element Meshes, Proceedings of 7th SIAM Conference on Parallel Processing for Scientific Computing, 1995, SIAM Press, Philadelphia, PA. p.633.

5. H.Q. Ding and R.D. Ferraro, A General Purpose Sparse Matrix Parallel Solvers Package, Proceedings of 9th Internal Parallel Processing Symposium,1995, IEEE Computer Society Press, Los Alamitos, CA. p 70.

6. J.C. McComb, G.A. Lyzenga, T.G. Lockhart, et al., 1993., unpublished JPL report.

7. H.Q. Ding, PGLIB: A Library of Partial Global Operations in Parallel Architectures. The source codes and brief description are in public domain and can be downloaded from Web at http://olympic.jpl.nasa.gov, click at Software Exchange.